2019

Design and optimisation of an additively manufactured patient-specific partial mandible reconstruction implant

Miriam Gerarda Esther Oldhoff

Master Thesis of

Biomedical Engineering

In Biomaterials and Tissue Biomechanics

TU Delft

Design and optimisation of an additively manufactured patient-specific partial mandible reconstruction implant

By

Miriam Gerarda Esther Oldhoff

in partial fulfilment of the requirements for the degree of

Master of Science

in Biomedical Engineering

at the Delft University of Technology,

to be defended publicly on Friday, December 13, 2019 at 11:00am.

Supervisor:	Dr. Mohammad Mirzaali Mazandarani	TU Delft
	Dr. Nazlli Tümer	TU Delft
	Prof. Dr. Amir A. Zadpoor	TU Delft

TU Delft

Acknowledgements

The manuscript in front of you is the result of over 8 months of work, which is the final step to obtain my master's degree in Biomedical Engineering. This project was accomplished with the help, supervision and support of many people, who I would like to extend my profound gratitude to.

First, I would like to thank Delft University of Technology for the absolute great experience and learning opportunities in the past 6 years, during both my bachelor's and master's degree. I would like to thank my daily supervisor, Mohammad Mirzaali Mazandarani, for his supervision and encouragement during my master thesis. He was always willing to help me by answering questions or giving advice. He pushed me to get the most out of this project. I would like to thank him especially for his confidence in me. Secondly, I want to express my appreciation to my additional supervisor, Nazli Tümer, who helped me during the project with her words of encouragement, great ideas and her amazing knowledge about statistical shape models. I am more than grateful for her help during the project and in the final weeks with her critical thinking that helped me improve my manuscript to present my finding in a more scientific and clear manner.

I also would like to thank the 3MED project (which received funding from the Interregg 2Seas programme 2014-2020, co-funded by the European Regional Development Fund under subsidy contract No2S04-014). Manuel da Silva Pinheiro, Anouar Krairi and Pim Pellikaan who's input, ideas and expertise helped me with the setup of the project and to create a finite element model for the mandible.

Similarly, I would like to thank the technical physicians and surgeon from the oral maxillofacial department of Amsterdam Medical Center. They helped me understand the clinical need and applications for both statistical shape model and mandibular reconstruction surgery. Their clinical expertise helped me to think more critically on the realistic use of partial mandible reconstruction implants and their ability to show me clinical cases improved my clinical perspective for the project.

Finally, my deepest gratitude to the people dear to me. My friends and fellow students who have been enormously patient and supportive these last few months, who always cheered me up and gave me the strength to carry on and put my worries into perspective. And most of all, my parents, who beside financially paying for my great education, have always been supportive and I would like to thank them for their endless love, support and faith in me. Mom and dad, this was all possible because of you.

Miriam Oldhoff,
Delft, November 2019

ABSTRACT

Additive manufacturing (AM) provides the opportunity for complex porous designs, without the costs depending on batch size. Therefore patient-specific implants can be rapidly manufactured. In clinical practice, reconstruction of the mandible is needed in case of bone tumors or trauma. Part of the mandible is removed and the shape of the missing part needs to be estimated, before an implant can be designed. Now-a-days the golden standard for mandible reconstruction is autograft surgery using the iliac or fibula bone. However, this comes with extra donor site surgery and asymmetrical face contours. Mandible movements are needed for mastication and speech and the mandible bone accounts largely for the individual's face appearance. Hence, good estimation is needed for both function and aesthetics

In this study, a statistical shape model (SSM) of the mandible was generated by segmentation of the mandibles from 35 full body CT-scans. The missing shape of the mandible was estimated using an extruded base, the SSM and mirroring of the intact side. Two finite element models (FEM) were made; one of a healthy mandible and one with a 25% total volume defect with a solid Ti-alloy implant created with the SSM. Two loading conditions were simulated separately; incision clenching (INC) and right molar biting (RMB). Topology optimizations were made with a volume constraint of 0.2 and 0.24 together with an objective function to minimalize the strain energy. To investigate more initial conditions, more topology optimizations were completed. These included one in which the initial implant included pores and two in which extreme mandible cases were used, which were retrieved using the b-values for the first mode of the SSM.

Variations in shape of the mandible were seen in the modes of the SSM. Mode 1 described the variations in shape between the intercondylar angle and distance, mode 2 of the gonial angle and symphysis length, mode 3 described the variations in shape and position of the condyle and mode 4 was associated with the coronoid process. Calculations of the maximum and average distances of the point cloud of the original missing bone part to the estimated shapes illustrated that both mirroring of the healthy side and SSM resulted in the closest estimation. No significance was found between the two methods. Limitations of the mirroring method in relation to the locations of the defects, resulted in the use of SSM for the design of the implant. Topology optimization resulted in optimized implant frames that were located at lateral inferior sides of the implants for both volume constraints and biting tasks. Small differences were seen in the exact location of the crossing of the implant frame. FEM results suggested correct maintenance of stress concentrations and displacements, when compared to the healthy intact mandible. It was suggested that the initial implant shape influences the optimized outcome. Different mandibles resulted in unique optimized implant frames, making the outcome patient specific. The workflow created in this study can be used as a proof of concept for the design and optimization of patient-specific implants for mandible reconstruction, which can easily be manufactured using additive manufacturing processes.

TABLE OF CONTENTS

LIST OF FIGURES

LIST OF TABLES

1

INTRODUCTION

Additive manufacturing (AM), widely known as 3D printing, has been used in medicine for several decades and classified into different applications for medical purposes [1] (*e.g.* medical models, aids, devices, implant or bio manufacturing). Clinical benefits of additive manufacturing include the ability to rapidly produce parts with complex geometries, increased patient care, reduced costs and better functional integration [2]. With AM, patient-specific implants that suit the patient's anatomy better can be manufactured at reasonable costs. In clinical practices such as bone related trauma or bone tumors, a reconstruction implant for missing bone is required. To come up with a proper implant design, the complete shape of the bone of interest should be estimated. However, how can a missing bone part be obtained and designed? The aim of this thesis study was to establish a semi-automatic workflow starting from post-processing computed tomography (CT) scans to a create an implant based on the patient-specific shape that is light weight and can be printed using additive manufacturing processes. For the proof of concept this workflow was tested using the mandible bone. The CT imaging was chosen as input, since it has the ability to fabricate detailed imaging slices of the bone tissue within the body among other things, allowing for three-dimensional (3D) modelling when combining these slices.

1.1 BACKGROUND INFORMATION

To understand the reconstruction of the mandible, the anatomy needs to be known. The mandible is U-shaped and is the strongest bone of the face [3]. Figure 1 illustrates the schematic anatomy of the mandible. The mandible includes the mandibular body and two vertical mandibular rami. The gonial angle (otherwise known as the mandibular angle) lays between the body and ramus. Every ramus has medial and lateral surfaces, four borders and two processes, which are separated with the mandibular notch [4]. The coronoid process, located anteriorly, is the attachment site of the temporalis muscles (figure 2) which elevates the mandible. Posterior to the coronoid process is the condylar process, also known as the

condyle, which is included in the temporomandibular joint (TMJ) and articulates with the glenoid fossa of the temporal bone. The TMJ is a bilateral joint and is one of the most frequently used joints of the human body. It is used for movements such as mastication, speech, snoring and kissing [5] and these movements take place up to 2000 times daily [6]. The joint's movement can be ginglymoarthrodial, meaning that it is both a hinge joint (ginglymus) and gliding joint (arthrodial) [7]. The TMJ allows for opening, closing, protrusion, retrusion and lateral deviation movements of the mandible [5]. The lateral pterygoid muscles attached on the condylar process allow for protrusion and lateral deviation movements of the mandible.

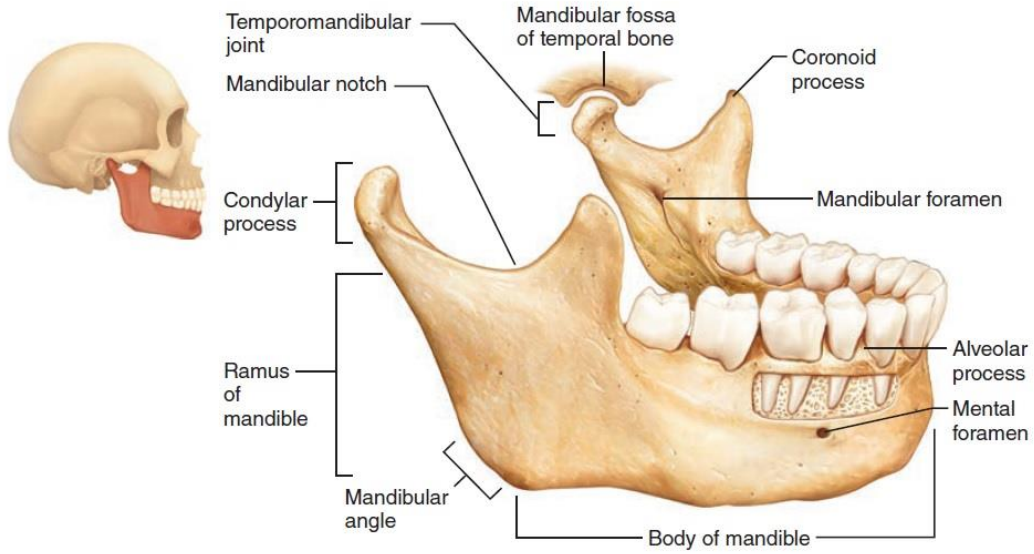

Figure 1: Schematic illustration of the mandible anatomy taken from literature [3] in right lateral view.

On the medial surfaces of the ramus is the mandibular foramina, where the mandible canal begins, which allows for the passage of nerves needed for tooth sensation. The mental foramina is located on the lateral side of the ramus, through which blood vessels and nerves can pass to skin around the chin [3]. The masseteric tuberosity is located near the gonial angle on the outer surface where the masseter muscle attaches. These muscles are the prime movers for closing of the mandible. The medial pterygoid muscles attached close to the medial surface of the gonial angle work together with the lateral pterygoid muscle to protract the mandible [3] and help with lateral deviation movements.

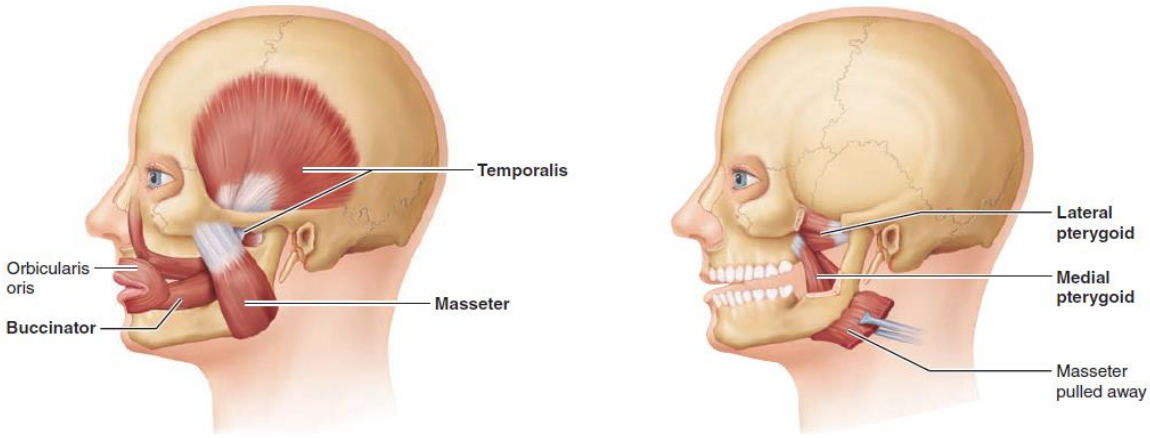

Figure 2: Schematic illustration taken from literature [3] showing the four main muscle groups (the masseter, temporalis, medial and lateral pterygoid muscles) for mandibular movement in left lateral view.

The mandibular body holds the lower teeth in sockets at its superior border which is called the alveolar process [3]. The midline of the body forms the mandibular symphysis, which forms the chin. The size and morphology of the mandible vary based on gender [8].

Mandibular bone loss can occur due to several reasons (*e.g.* trauma, inflammatory diseases or tumors) following which mandible reconstruction is needed [9]. Trauma can be caused by assaults (*e.g.* fist fights, beatings with blunt objects and gunshot wounds), falls, motor vehicle-, bicycle- or sport accidents [10, 11]. Majority of these trauma patients are male [10, 11]. Since the mandible is used frequently for essential daily activities and accounts for the contour of an individual's face, proper reconstruction is preferred.

Reconstruction of the mandible has been done by several techniques over the last century. These include surgery with free bone grafts, pedicle bone graft, particulate bone cancellous marrow graft, reconstruction plates and microvascular free flaps [9]. The golden-standard now-a-days is Iliac- and fibular- free flaps, whose selection depends on several factors [12] (e.g. premorbid state and size and location of the reconstructed part). The iliac crest is recommended for defects on the gonial angle or mandible body, whereas fibula flab is suggested for cases where longer donor bone segments are needed [12]. However, this comes with extra donor site surgery, resulting in extra surgery time, costs and discomfort for the patient. Additionally, auto graft surgery can lead to asymmetrical unwanted shapes which have a big influence on the physical appearance of an individual's face.

A statistical shape model (SSM) is created by examination of a dataset with training shapes, which are obtained from 3D models created by segmentation of CT scans. Using principal component analyses (PCA), a 3D bone shape of the studied population can be described with

a mean shape and the primary modes of variations [13]. Using a SSM, the variations of the mandible of the database used in this thesis was investigated. Additionally, the SSM can be used to estimate the shape of the missing anatomy of the mandible, which can then be used for the design of patient-specific mandible implants.

Topology optimization was described by Martin P. Bendsøe as ' *structural optimization where the choice of design variable allows for a prediction of a general distribution of material in space'* [14]. It minimalizes a certain objective, with no constraints prior assigned on the topology [14]. Two different constraints were used; one accounted for the volume fraction for weight reduction purposes and the other was assigned as a frozen area. This frozen area was located at the outer contours at anterior and posterior borders of the implant for a rigid connection to the remaining bone. Additionally, the inferior and superior borders of the implant were assigned to the frozen area as well, to preserve the estimated shape of the missing anatomy of the mandible using the SSM. The focus of this thesis was on global topology, not on local structures of porous scaffolds.

1.2 RESEARCH QUESTIONS

The motivation behind this study was to come up with a semi-automatic workflow for designing a patient-specific implant for partial mandible reconstruction surgery. This workflow could be extended for the design of implants at other anatomical locations. The research questions of this study were defined as the following:

1. What steps need to be taken to create a statistical shape model (SSM) of a human mandible?
2. Can differences be seen within the variations observed in the SSM for age and gender?
3. How can a SSM be used for a partial mandible reconstruction implant?
4. What is the accuracy of using a SSM in estimating the shape of the original bone part and is this superior to the use of an extruded base or mirroring of the intact side?
5. How does the global topology optimization change with different boundary conditions for different biting tasks and with different initial constraints?
6. Does the shape of the topology optimized outcome differ between patients and can it therefore be assumed to be patient-specific?

1.3 STUDY OUTLINE

To find answers to the research questions, several steps were taken, including segmentation of 35 mandibles to create a statistical shape model (SSM). Then the SSM, mirroring and an extruded base were used for estimating the shape of a missing bone part for different defects scenarios to investigate if the use of SSM was superior to less complicated methods. The point clouds of these designed parts were compared to a point cloud of the missing bone part. This was done to measure the maximum distance and average distance of the two points clouds. One implant was then made for a 25% total volume defect located at the mandibular body, since this is one of the most common mandibular defects [15, 16] and no muscle attachments were included. A finite element model (FEM) was made for two different loading conditions and applied on two models. One was a fully intact mandible model with no previously known pathologies, referred to in this thesis as the healthy mandible, and the second model was a mandible including a solid titanium alloy implant for a 25% volume defect. Topology optimizations of this implant were done for weight reduction purposes using several loading conditions and volume constraints. Finally, the mandible model and its designed implant were additively manufactured for visualization purposes.

2

MATERIALS AND METHODS

The materials and methods used in this study are covered in this chapter. Figure 3 illustrates the steps employed from the initial step of data collection to the final 3D printed model. The first part of the chapter describes the data collection and segmentation processes needed for the statistical shape model (SSM). The fabrication of the SSM is explained, followed by statistical analyses. Several defects scenarios were created. Finite element models (FEM) were made for the heathy model and a 25% volume defect. Topology optimization was also carried out for different scenarios. Finally, both the healthy model and the topology optimized implant model were additively manufactured.

2.1 DATA COLLECTION

A total of 35 mandibles with no known existent pathologies were included in this study, obtained from an anonymized database. Only gender and age (14 male, mean age: 31.4 years, SD= 6 years; 21 female, mean age: 32 years, SD= 6.5 years) were known. The CT database of full body images was retrieved from a previously used database published in literature [17]. The CT scans were taken at Utrecht Medical Centre (UMC) between 2011 and 2015 and were acquired using a 40 detector row CT scanner (LSO PET 40-slice CT scanner, Siemens healthcare, Erlanger, Germany). Additional acquisition parameters were collimation of 40 x 0.6 mm, tube voltage of 120 kVp, the effective dose was 10 mAs, rotation time of 0.5 sec and slice thickness of 1.5 mm [17]. Matrix sizes of 512 × 512 (n= 32) and 1024 × 1024 (n=3) were used. Voxel sizes were around 1.0 mm × 1.0 mm × 0.75 mm.

2.2 SEGMENTATION

The mandible was segmented from each CT scan using Mimics (version 21.0, Materialise, Leuven, Belgium). The CT images were cropped from a full body scan to a CT scan image set only including the oral and maxillofacial region. The segmentation was first done using a threshold for bone (Hounsfield Unit > 225), after which the mandible was separated from the cranium and

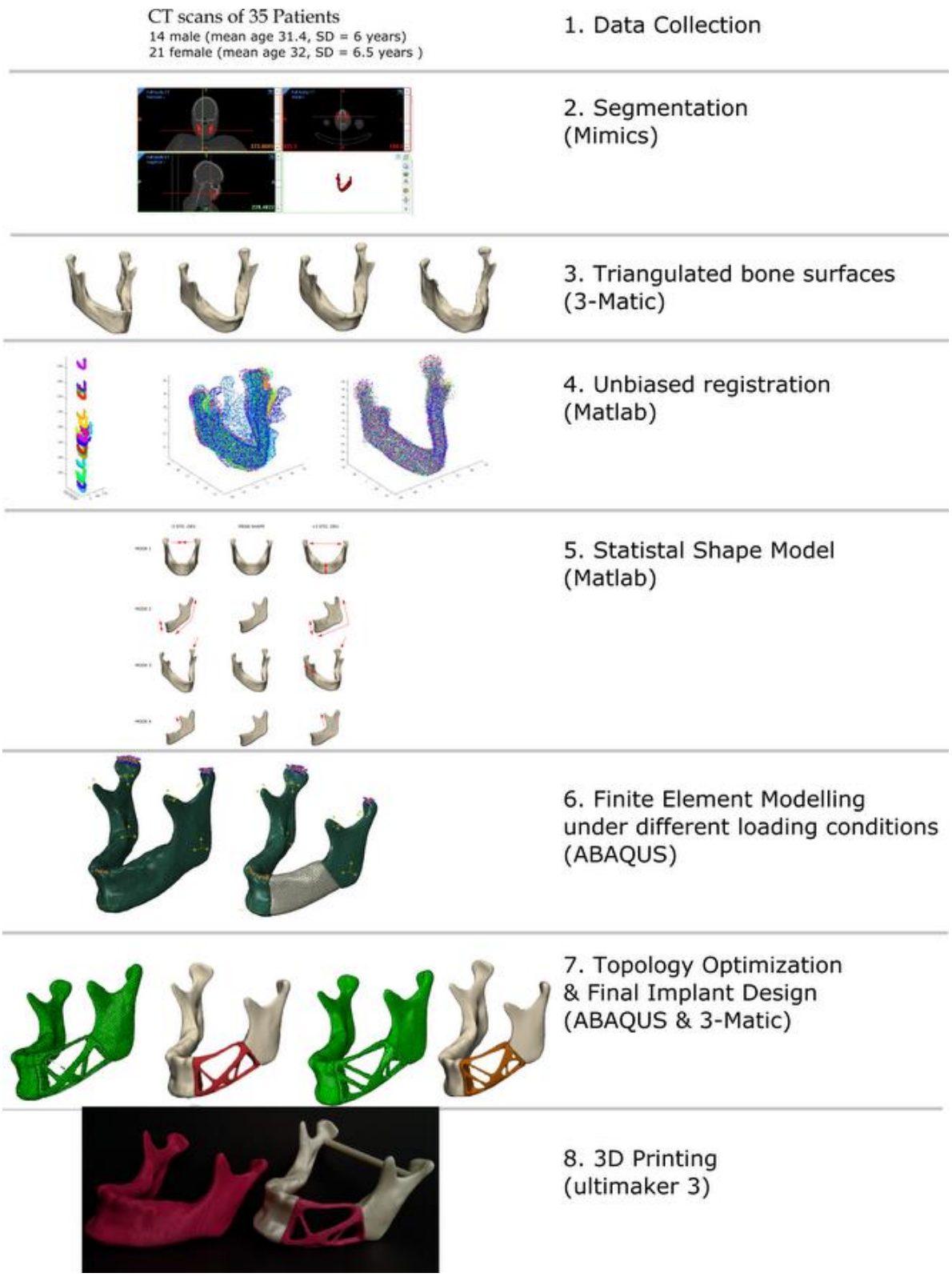

Figure 3: General scheme of going from a CT database to an additive manufacture mandible implant with topology optimization.

teeth using region grow and split mask options. Finally, edit mask options were used to manually correct the mandible separation from the cranium and for small inaccuracies, such as flaws created by metal artifacts and teeth. The created segmentation mask was calculated to a part, every slice was manually checked again and potentially adapted using 3D tools to edit the contours. This was done to assure smooth but accurate transitions between slices, while all bony contours were still considered. Only outer contours were included, meaning that the porosity of bone was not taken into account for the SSM. The teeth region was neglected and therefore also not taken into account. Using the same software (3-matics), extra local smoothing and uniform remeshing with a maximum triangle length size of 0.5 mm was assigned such that all small anatomical features were included. These triangulated surfaces were exported and used as inputs for the SSM.

2.3 STATISTICAL SHAPE MODEL (SSM)

The SSM was created using similar approaches as previously reported [17-19] by first using an unbiased registration algorithm [20] with point clouds. The mean shape was obtained by registrations of an initial estimated mean shape to point clouds from the SSM mandible database. After the registration, the mean shape was deformed and updated. The final mean shape was based on all those updated estimates. Each point cloud for registration of the mean shape includes 3000 points, which were randomly chosen over the surface, to assure all anatomical features of the mandible would be considered. The alignment of all 35 mandibles took place by translation and rotation to assure all point clouds were in a similar position, scaling and orientation. Firstly, they were translated to the origin of a common coordinate system, following which they were scaled to the unit centroid size [19].

The total number of points used in every model was approximately 3.5 times the surfaces area [mm], resulting in a mean amount of points of 66230 (range: 49293 – 90168, SD: 9956,56). Principal component analyses (PCA) were performed on the covariance matrix of the data factor (the size of the data vector was 85344 x 3 x 35), to extract the eigenvectors and eigenvalues for each bone, representing the modes of variation and variances respectively. With the mean shape, the eigenvalues and eigenvectors, a new mandible shape ($\mathbf{x}$) can then be described with the following equation (1).

$$\boldsymbol{x} = \hat{\boldsymbol{x}} + \sum_{\boldsymbol{n=1}}^{\boldsymbol{c}} \boldsymbol{b_n \phi_n} \qquad (1)$$

$\hat{\boldsymbol{x}}$ represents the SSM mean shape and $\boldsymbol{\phi}$ is the matrix including the modes of shape variations (*e.g.* eigenvectors). The *b*-values, otherwise known as the shape parameters, defines the amount of influence of the modes on the mean shape. Differences between the mandible bones are therefore described with this $\boldsymbol{b}$ vector. For example, b_1 for ϕ_1 will describe the distance of mandible $\boldsymbol{x}$ to the mean shape $\hat{\boldsymbol{x}}$ for the first mode. The sum of the contribution of all modes and the mean shape will make up the new mandible shape.

2.4 STATISTICAL ANALYSES

Since this SSM was built on a dataset, which was a mixture of female and male mandibles and the mean shape ($\hat{\boldsymbol{x}}$) and the modes of variation ($\boldsymbol{\phi}$) are therefore equal for both genders, the shape parameters can be compared to see if male and female had significant differences in the variations of SSM. This was done to see if a gender specific SSM was needed. All statistical analyses were performed done using SPSS (version 25, Chicago, IL).

Firstly, the assumption that age is normally distributed for male and females was assessed with the Shapiro-Wilk test. The independent-sample t-test was used to determine if there is a differences in age and between male and female. A MANCOVA analysis was performed to investigate the significant differences between male and female for the first 10 b-values, including age as covariate in the test. In the analyses the first 10 b-values were included, since modes higher that mode 10 account for less than 2% of the final shape. Using the Bonferroni correction, the significance level was changed from P=0.05 to P=0.005 (*i.e.* 0.05/10 modes).

2.5 IMPLANT DESIGN

From this point in the study, one mandible was selected from the database, whose shape was closest to the mean shape of the SSM. To determine this, the absolute b-values for the first 10 modes were multiplied with their respective contribution to the overall shape ($\%_{\text{mode i}}$), shown in equation (2). The patient with the lowest total score represented the mean shape of the population, which belonged to a 33-year-old male.

$$\boldsymbol{score} = \sum_{\boldsymbol{i=1}}^{\boldsymbol{10}} \boldsymbol{abs}(\boldsymbol{b_i}) \times \%_{\boldsymbol{mode\ i}} \quad (2)$$

To find the best method that would suit the process of estimating the shape of the missing anatomy, three different methods were attempted. These were the SSM, mirroring of the healthy intact side of the mandible and the use of an extruded base. The mandible was manually adapted to investigate several defect scenarios.

To visualize the defects scenarios, the model was modified four separate times using 3-Matic Research 13.0 (Materialize, Belgium), each time removing a specific segment of the mandible. The planes used to cut the model were perpendicular to the surface, but not taken at specific anatomical landmarks. Variations of the defect scenarios were defined by different percentages of the missing volume. The removed part represented the reconstruction area of the mandible where the reconstruction implant should be placed. Figure 4 shows these four modified models. Models A to C have 10%, 25% and almost 50% of the total volume defects, respectively. Model D represents a defect of the symphysis of 16% of the volume of the mandible. By the classification of Urken et al. [16], model A visualizes a small body defect, model B a larger body and partly symphysis defect, model C a ramus body symphysis defect and model D a symphysis defect.

To investigate the accuracy of the designed part, the maximum and average distances of the implant were measured with respect to the manually removed missing bone part using CloudCompare (open software, [21]). The point cloud of the original missing bone shape was compared to the shape of the extruded base, the mirroring shape and the estimated shape using SSM. These comparisons were done for all defect scenarios. Additionally, four other mandible models were chosen and implants for all four defects were made using the selected methods, to investigate the maximum and average distance for five mandibles in total. These five cases included the mandible model closest to the mean shape, models with smallest and largest b-values for mode 1 of the SSM and two randomly selected mandibles from the database. Statistical analyses between the maximum and average distances were carried out with independent- sample t-tests using SPSS (version 25, Chicago, IL).

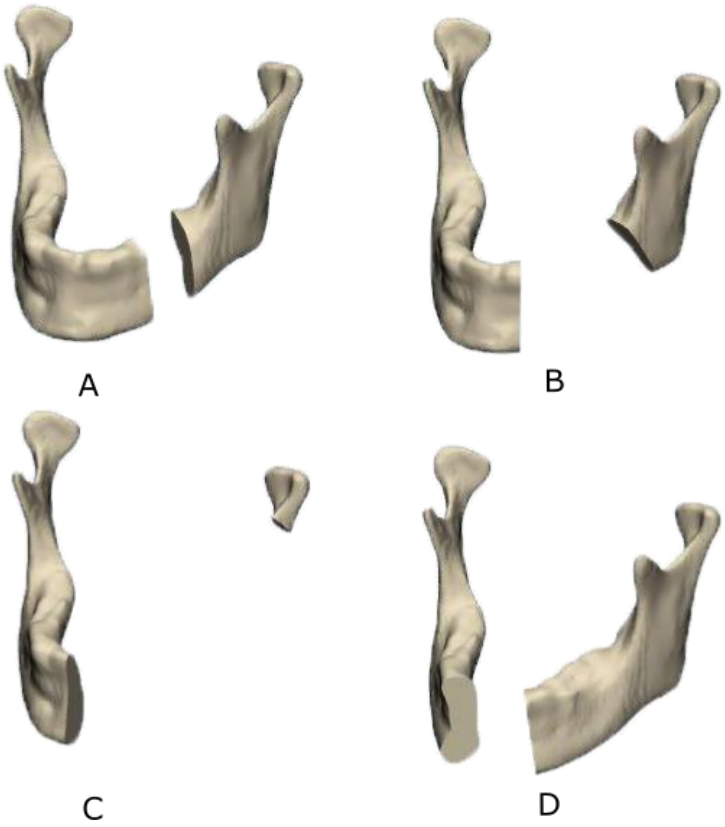

Figure 4: Manually made defects of 10% (model A), 25% (model B) , 50% (model C) and chin/16% (model D) of the total volume of the intact mandible.

2.6 FINITE ELEMENT MODELLING (FEM)

For the FEM of the mandible, the global coordinate system was assigned as follows; x-axis was positive in lateral direction to the left side of the mandible, taken from mandibular symphysis. Y-axis was positive in superior direction perpendicular to the x-axis and the z-axis was obtained from both previous axes and perpendicular to both. Positive z direction was therefore anteriorly. The origin of the coordinate system was at the symphysis of the mandible. All FEM were made using the commercially available software ABAQUS, version 2017 (Dassault systems, Vélizy-villacoublay, France).

2.6.1 Material Properties

Grey values for both the cancellous bone and cortical bone were retrieved from CT-data and used to calculate the material properties. These properties were assigned to the mean model using Mimics research 21.0 (Materialize, Belgium). The grey values were obtained using Hounsfield Units (HU), which uses electron density and is described as follows:

$$HU = 1000\left(\frac{\mu - \mu_{water}}{\mu_{water}}\right) \quad (3)$$

μ_{water} and μ are the linear attenuation coefficient of water and a material, respectively.

The HU values within the FEM model for the mean shape ranged from -131 to 1677. The first material properties were assigned for a section of HU values < 0, to prevent negative density values. These negative HU values occur because of porosity of bone. The linear attenuation coefficient at these porous bone sections was smaller than water, resulting in a negative HU value. A lower limit for the density and minimum Young's Modulus and Poisson's ratio were taken for these sections, using equations (4) and (5), as p=0.105 g/cm^3 and E=0.06 GPa. The Poisson's ratio of v = 0.3 was assigned to all bony elements in the FEM.

Density (ρ) and Young's modulus (E) for the mandible were calculated using equations mentioned in literature [22]. For both cancellous and cortical bone, 10 sections were assigned individually. For cancellous bone, values of 0 < HU < 816 were taken and material properties were calculated using the following equations [22]:

$$\rho = 0.015 + 0.0019HU \quad (4)$$

$$E = 0.06 + 0.9\rho^2 \quad (5)$$

For cortical bone, values of HU ≥ 816 were taken and material properties were calculated using the following equations [22]:

$$\rho = 1.028 + 7.69 \times 10^{-4}HU \quad (6)$$

$$E = 0.09 + 0.9\,\rho^{4.53645} \quad (7)$$

This resulted in ρ-values ranging from 0.184 to 1.56 g/cm^3 and E-values ranging from 0.091 – 2.31 GPa for cancellous bone, ρ-values ranging from 1.69 to 2.32 g/cm^3 and E-values ranging from 9.84 - 40.70 GPa for cortical bone. The results for all material sections, including the number of elements of each section, are reported in table 9 in appendix A. Material properties are reported separately for the healthy intact mandible and the model including

the solid titanium implant. For the healthy model, the mean Young's modulus for cancellous and cortical bone were 0.97 GPa and 18.8 GPa, respectively. For the model including the implant, the mean Young's Modulus for cancellous bone and cortical bone were 1.0 GPa and 18.4 GPa, respectively.

The mechanical properties of a biocompatible titanium alloy, Ti-6Al-4V, were assigned to the designed implant as E=113.8 GPa, $\nu = 0.34$ and $\rho=4.43$ g/cm^3 [23].

2.6.2 Forces and Boundary Conditions

FEMs were made for two loading conditions, incisal clenching (INC) and right molar biting (RMB), and boundary conditions for both cases were taken from literature [24, 25]. To simulate an incision bite, the mandible was restricted in the superior-inferior direction (U2=0) at the first four incisors, which are the four front teeth. To simulate the RMB, the first and second molar were restricted in the superior-inferior direction (U2=0). Additionally, both condyle superior surfaces were restrained in all directions for both cases, simulating fixation by the skull.

Force directions were taken from [25] for four muscles each side, representing the three major muscles groups for the mandible movement. These included the masseter muscle, temporalis muscle and both the medial- and lateral pterygoid muscles. Pinheiro et al. [23] combined the single tooth forces of [26] for male for the different clenching tasks. Adding the tooth forces of the four incisors used for the INC task resulted in a reaction force of 570.9 N. Combining the tooth forces of the first and second molar used for the RMB task, resulted in a reaction force of 600.4 N. The muscle forces were scaled to match these reaction forces and these were used for both simulations in this study. The muscle magnitudes of the scaled forces applied by the four muscles and their directions are reported in table 1, directions of the forces of [23] were changed to match the coordinate system of this thesis study. Each force was applied to one node on the surface of the model. This node was constrained to several slave nodes by multi point constraints (MPC) using the rigid beam option. This MPC was used to constrain the displacement and rotation of the selected node to several closely surrounding nodes on the surface, allowing for the force to be more contributed over the mandible surface. Locations of the muscle attachment are shown in figure 5. For simplicity, muscles are shown on either left or right side of the mandible, however these muscle attachments occur on both sides and are in opposite x-direction.

Table 1: Muscle forces in all three directions taken from Pinheiro et al. [23]

	INCISION CLENCHING (INC)			RIGHT MOLAR BITING (RMB)		
Muscle	Force x-direction [N]	Force y-direction [N]	Force z-direction [N]	Force x-direction [N]	Force y-direction [N]	Force z-direction [N]
right masseter	-123.0	375.4	109.4	-78.6	215.4	47.4
left masseter	123.0	375.4	109.4	65.5	179.5	39.4
right temporalis	-17.0	84.3	-22.0	-52.6	244.3	-84.0
left temporalis	17.0	84.3	-22.0	44.3	205.6	-69.2
right lateral pterygoid	183.8	-32.4	203.5	16.4	-4.5	19.8
left lateral pterygoid	-183.8	-32.4	203.5	-35.6	-9.8	42.8
right medial pterygoid	298.2	485.3	228.9	92.8	151.0	71.5
left medial pterygoid	-289.2	485.3	228.9	-66.3	107.8	50.9

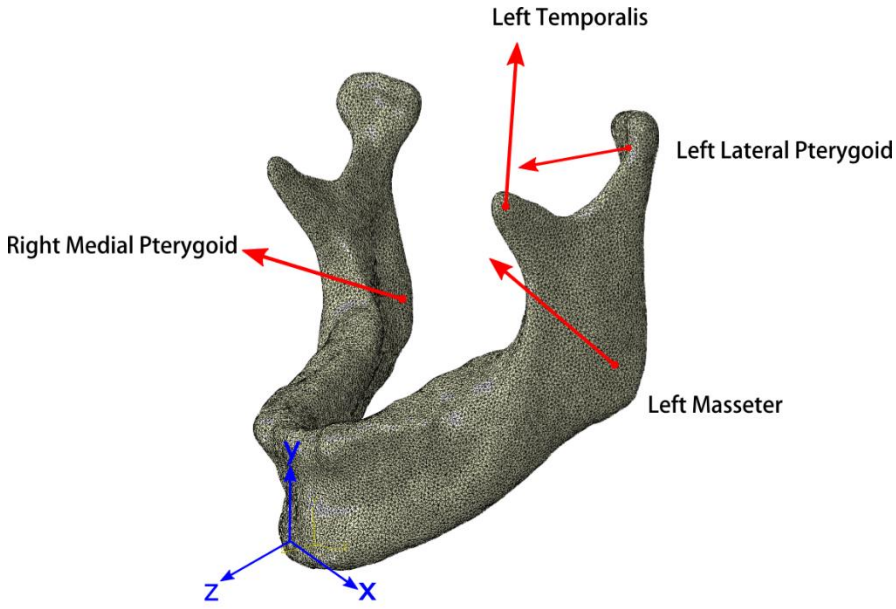

Figure 5: Simple representation of the four main muscles involved for the simulation of human clenching and biting tasks. All four muscles can be found on both left and right side.

2.6.3 Model

The FE models of the mandible simulating INC and RMB tasks were prepared in ABAQUS (figure 6). The healthy bone model on the left of figure 6 has a maximum triangle length of 0.5 mm to create a model that is realistic, since this was lower than the slice thickness of the CT-scan. As on seen the right of figure 6, remeshing caused some changes in the geometry of the mandible, such smoothing of the surface. However, due to larger simulations in future steps for the topology optimization, which require large calculation time, mesh size was increased to a maximum length size of 2.0 mm in the model including the implant. Remeshing the mandible with 2.0 mm resulted in volume and surface fraction of 0.99 with respect to the mandible with maximum of 0.5 mm triangle length. The total number of elements for both cases and their parts are shown in table 2. All parts were meshed with a quadratic tetrahedral elements of type C3D10. The implant and bone were connected with a tie constraint, in which the connected implant surface was the master surface and the surface to which it was attached on the bone was the slave surface [27].

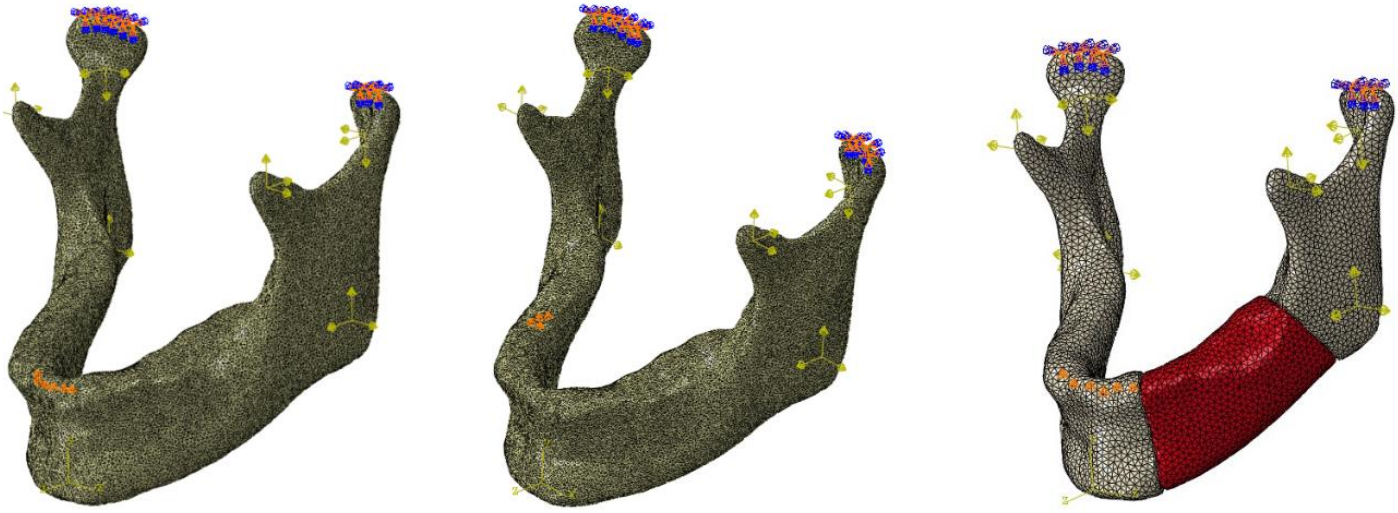

Figure 6: FEM of the healthy mandible with INC boundary conditions (left) and RMB boundary conditions (middle) and that of the modified model with a solid titanium alloy implant with INC boundary conditions (right) in ABAQUS (Dassault systems, Vélizy-villacoublay, France).

Table 2: Number of nodes and elements per part for both models.

Model	Part	Type of mesh	Nodes	Elements
Healthy model	Bone	C3D10	992 227	717 938
Implant model	Bone	C3D10	295 370	216692
	Implant	C3D10	92 634	68424

2.7 TOPOLOGY OPTIMIZATION

In this study, topology optimization was done using ABAQUS using the optimization tasks module. The optimization on an initial implant design was realized considering strain energy (SE) and total volume. These were assigned in ABAQUS as design responses. The volume was used as a constraint, in which the maximum volume fraction was determined prior to the simulation. The objective function included the strain energy, which was to be minimalized. The measure for this was defined in ABAQUS as equation (8), the vector **u** represents the displacement of the nodes and matrix **k** represents the global stiffness. A simplified equation for this is given in equation (9), using Young's modulus (E) and stress (σ) for each element. Minimalizing the strain energy means maximizing the global stiffness.

$$\boldsymbol{SE} = \sum \boldsymbol{u^t k u} \tag{8}$$

$$\boldsymbol{SE} = \frac{\mathbf{1}}{\mathbf{2}} \frac{\boldsymbol{\sigma^2}}{E} \tag{9}$$

A geometric restriction was assigned as a frozen area. The set of elements for this is shown In figure 7. Elements selected were the surfaces where the bone connected to the implant and to the superior and inferior borders of the implant. Hence, the estimated shape retrieved from using SSM would stay untouched. This way the benefits from using SSM, meaning the accurate jawline, were still obtained in the optimized shape. Several layers of elements from the contour inwards were selected, to assure the final results from topology optimization was decent enough to modify and print. Superior and inferior borders had a width of around 3 mm, while the anterior and posterior surfaces had a width of around 5 mm. The set consisted of 5900 elements (*e.g.* the whole solid implant consisted 68424 elements).

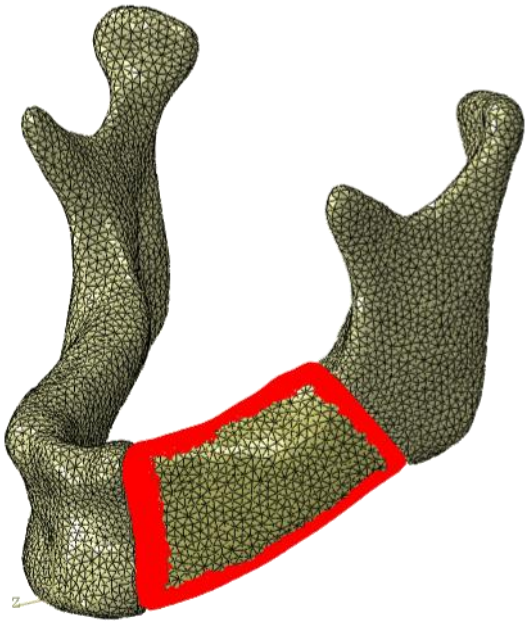

Figure 7: Frozen area constraint of the solid implant in Abaqus for topology optimization.

The optimization was done iteratively. The design constraint was set as 0.24 fraction of the initial volume, to create an implant with around the same weight as the manually removed bone part. Since the frozen area was already assigned for a part of the design constraint regarding the maximum volume of the optimized implant, a lower value for the volume constraint that would match the stiffness of the bone better was not realistic. The minimum of this constraint was found to be around a fraction of 0.2 of the volume. A maximum of 35 cycles was allowed for the topology optimization. INC was simulated for both cases, while the topology optimization with the conditions for RMB was only done with the minimal volume constraint of 0.2.

The final outcomes for the mean shape model were exported as STL-file from ABAQUS. This STL-file was imported to 3-matics where it was manually adapted to create an appropriate STL-file for 3D printing, by first cutting the implant out of the result and then using the local smoothing tool and remeshing to improve rough surfaces created due to the mesh size. However due to this, the shape and size were slightly different than the outcome of the topology optimization tool. The volume of the smoothed and remeshed implant was 0.9 of the initial volume resulted from the topology optimization tool.

The modified implants were remeshed with a maximum triangle size of 2.0 mm, implemented in ABAQUS and tested under other loading conditions. Mastication takes place using different biting and clenching techniques and the implant should therefore function

under all loading conditions. This means that the topology optimized implant created under the INC task (TI_INC) was tested under RMB conditions and the implant created under the RMB task (TI_RMB) was tested under INC loading conditions.

Next, three regions of the left side of the mandible were investigated for average von Mises stress and the maximum von Mises stress. These regions were taken as a slice from the condyle neck, a slice from the coronoid process and a section of the gonial angle. The measurements were taken from the healthy model under INC (healthy_INC), healthy model under RMB (healthy_RMB), the TI_INC under INC (TI_INC_INC), the TI_INC under RMB (TI_INC_RMB), the TI_RMB under INC (TI_RMB_INC) and the TI_RMB under INC (TI_RMB_RMB). Results were compared to check if similar stress concentrations occur with the topology optimized implants.

To investigate if pores in the initial design of the implant influence the topology optimized outcome, another FEM for topology optimization was made in which holes were created by removing several elements of the mesh. A total of 15 pores were created in the lateral/medial direction and an additional four were created in superior/inferior direction (figure 8). The new mesh of the implant included 9263 elements and had a volume of 16071 mm^2, resulting in a 0.85 volume fraction of the original solid implant. Due to this volume, a new volume constraint of 0.24 was assigned to have similar outcome in volume as the topology optimization completed with the solid implant.

Lastly, to investigate if patterns differ in extreme mandible shape cases, two more topology optimization tasks were completed. FEM of two other mandibles retrieved from the patient database were built following the previously described steps. One of the mandible shapes had the smallest b-value (-2.12) for mode 1, the other mandible shape had the largest b-value (+2.12) for mode 1 (appendix C). Muscle forces and boundary conditions were taken for the INC task.

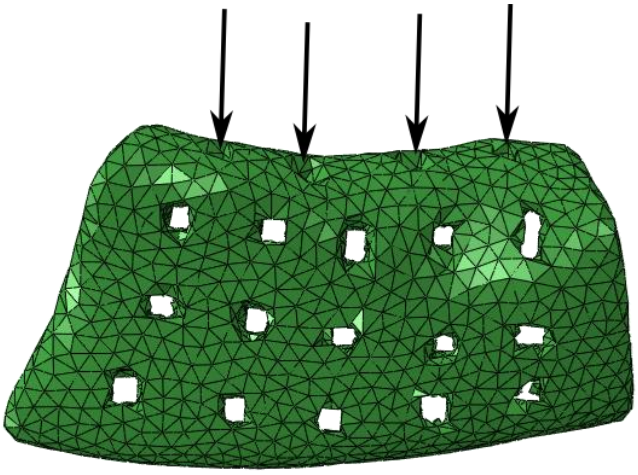

Figure 8: Pores created by removing elements within the mesh to investigate if this had an influence on the final topology. The black arrows point out the pores created at the top of the implant.

2.8 PRINTING

The healthy intact mandible, the mandible with the 25% volume defect and topology optimized implant under INC with the volume constraint of 0.2 were printed for visualization purposes. The additive manufacturing technique used was fused deposition modeling (FDM), in which a continuous semi-liquid thermoplastic polymer filament is used to form layers [28]. The machine used was the Ultimaker 3 3D printer (Ultimaking Ltd., Geldermalsen, Netherlands) in combination polylactic acid (PLA) filament.

3

RESULTS

In this chapter, results of the statistical analyses carried out for age and gender, the variations in shapes of the statistical shape model (SSM), measurements of the mean shape of the SSM and the mandible used for further steps, the estimated shapes and their distances to the original shape, FEM results and the topology optimized outcomes are presented. Finally, figures of the additively manufactures models are shown.

3.1 STATISTICAL ANALYSES DATABASE

There were 14 males (mean age: 31.4 years) and 21 females (mean age: 32 years) included in this study. To determine if there was a difference in age between males and females, an independent-samples t-test was run. Age was normally distributed for both males and females, as assessed by Shapiro-Wilk's test (p=0.159) and there was homogeneity of variances, as assessed by Levene's test for equality of variances (p=0.632). No statistically significant difference (p=0.778) was found in age between males and females. Figure 9 illustrates the distribution of age for male and female using box plots, showing that age was slightly more widely distributed for female.

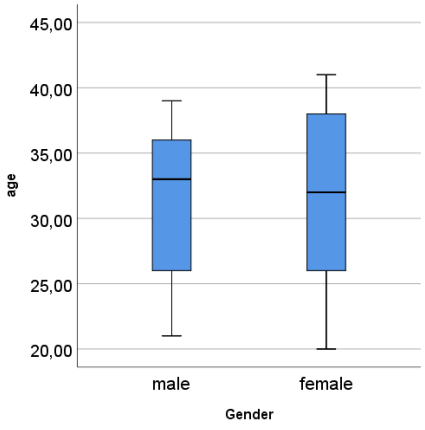

Figure 9: Box plot of age versus gender.

3.2 STATISTICAL SHAPE MODEL

All 35 stereo lithography (STL) files in isotropic, anterior, superior and lateral views are shown in appendix B. The contribution to the overall shape of the mandible of the first 10 modes is reported in table 4. The first 4 modes accounted for almost 60% of all shape variations in the mandible while modes higher than 4 accounted each for 5% or less. Therefore, the first four modes and their -3 and +3 standard deviations (STD DEV) are shown in figure 11 and these variations can be described as follows:

- The first mode was mainly associated with the lateral distance between both condyles. The distance increased when standard deviations moved from -3 to +3.
- The second mode was mainly associated with the gonial angle and the length of the symphysis. The gonial angle decreased, while the length of the symphysis increased as standard deviations moved from -3 to +3.
- The third mode was associated with the shape of the condyle, the width of the ramus and in small portions the gonial angle and symphysis length. The size of the condyle increased and the condyle turned inward, while the width of the ramus increased when standard deviations moved from -3 to +3.
- The fourth mode was associated with the variance of the shape and size of the coronoid process. The length of the coronoid process increased and pointed more upwards when standard deviations moved from -3 to +3.

Table 3: The contribution per mode for the first 10 modes of the SSM.

MODE									
1	2	3	4	5	6	7	8	9	10
24.14%	18.89%	9.42%	7.31%	5.08%	4.03%	3.83%	3.13%	2.82%	2.24%

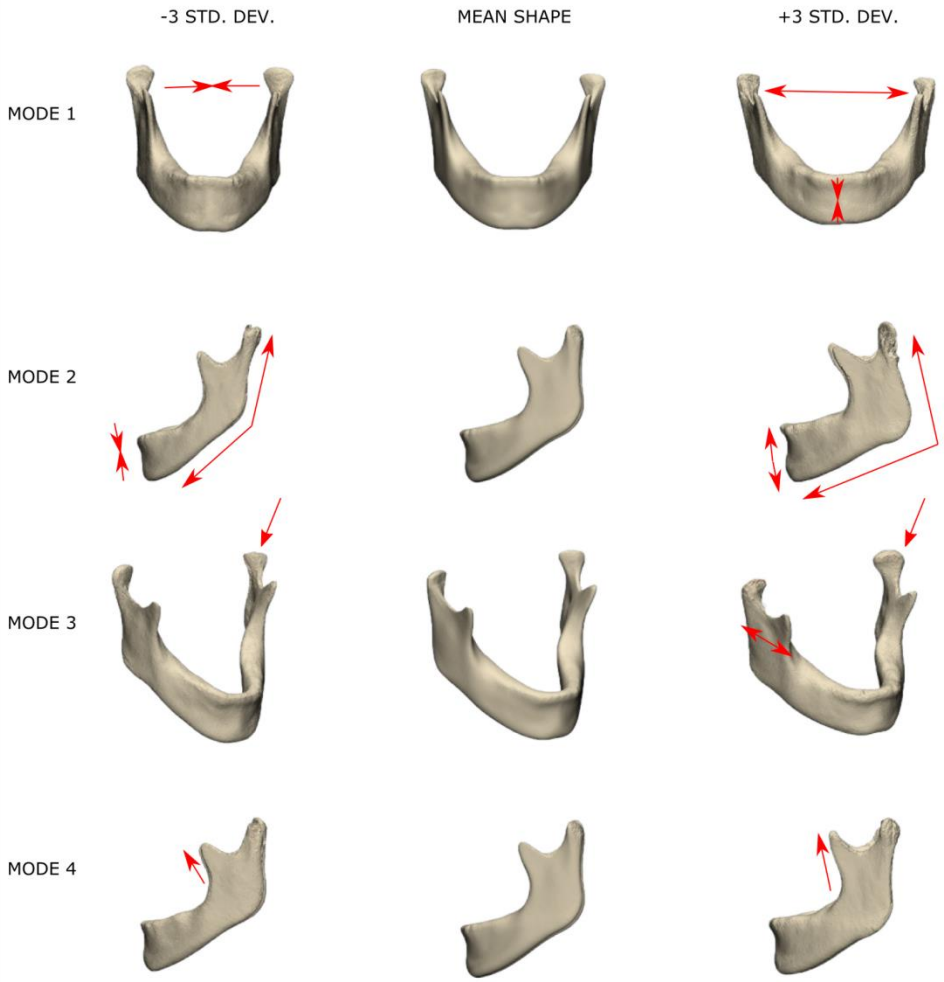

Figure 10: Shape variations that are described by the first four modes of the SSM, red arrows display the main shape changes in the mandible.

3.2.1 Statistical Analyses SSM

A MANCOVA was performed to investigate the effect of the B-values for male and female. All p-values (table 3) were greater than 0.005, which is the adapted p-value using the Bonferroni correction, meaning that none of the first ten b-values were statistically significantly different between male and female mandibles. The b-values for the first four modes, are plotted in figure 10 for both male and female.

Table 4: p-values resulting from MANCOVA analyses for the first 10 b-values with regard to gender using SPSS.

	b1	*b2*	*b3*	*b4*	*b5*	*b6*	*b7*	*b8*	*b9*	*b10*
P	0.030	0.099	0.155	0.749	0.574	0.803	0.058	0.228	0.473	0.645

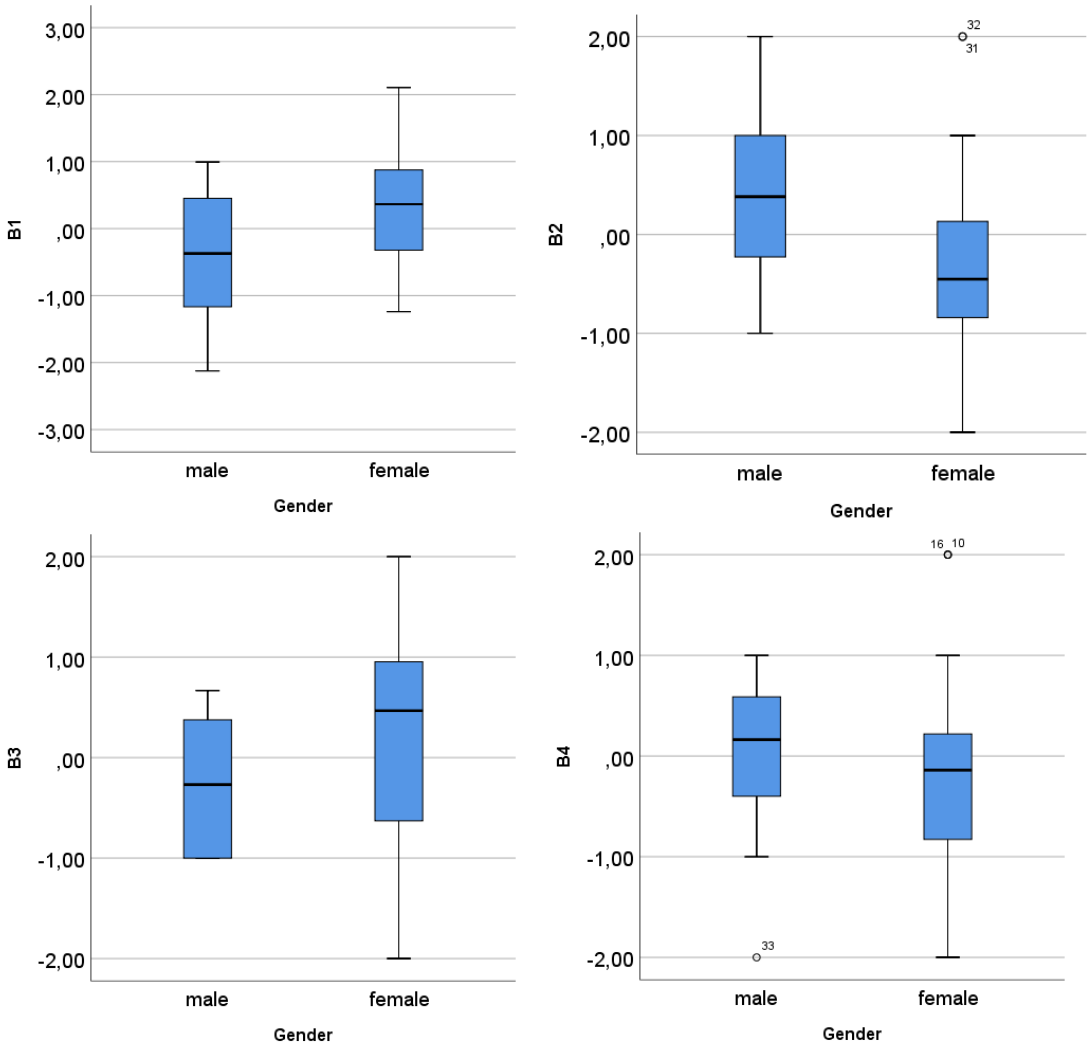

Figure 11: Box plots of the (b-values) represented for both male and female for mode 1 (top, left), mode 2 (top, right), mode 3 (bottom, left) and mode 4 (bottom, right) of the SSM.

3.2.2 Measurements

On the mean shape of the SSM, twelve measurements were obtained using twelve anatomical landmarks, which are shown in figure 12. More detailed descriptions on these landmarks and morphometric measurements are given in literature [8]. The measurements for both the mean shape of the SSM and those of the model used in the future steps of this study are given in table 5. Additonaly, the SSM measurement results of Vallabh [8] for both male and female mandibles are added as a reference. Measurements for the model used in future steps of this thesis are taken for the right side, however these are not similar to the left side of the mandible due to assymetry.

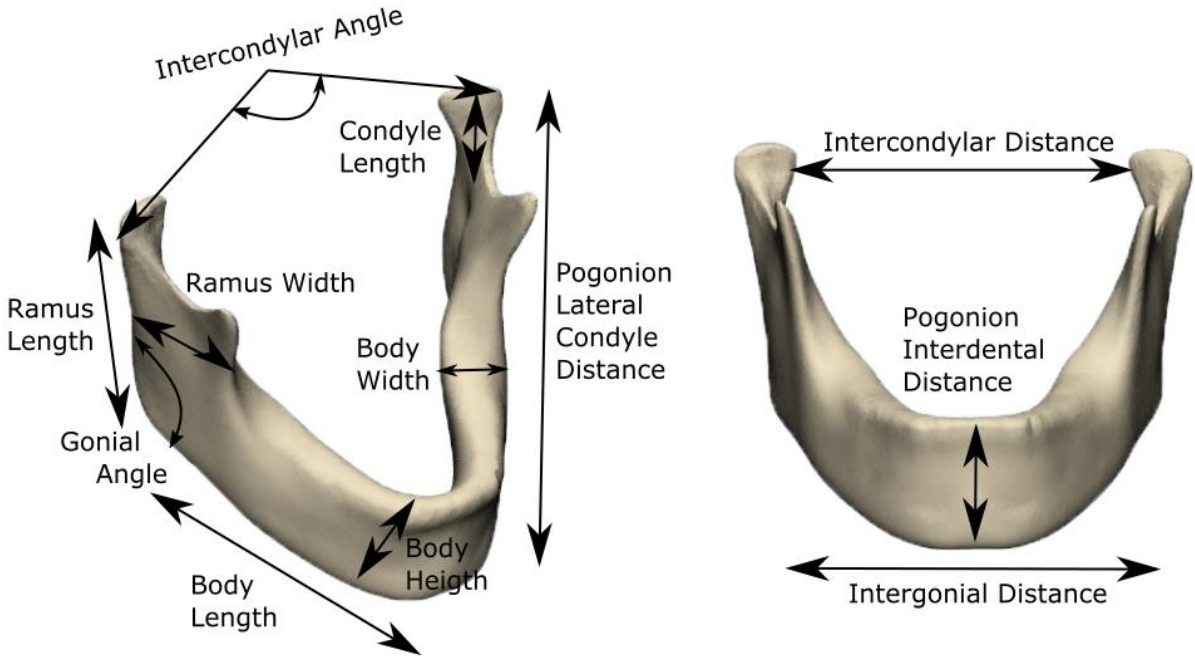

Figure 12: Twelve morphological measurements reported in Table 5.

Table 5: The twelve morphological measurements of figure 12 measured in mm for the mean shape of the SSM, the mandible used in this thesis and the mean shape of the SSM of female (F) and male (M) reported in literature [8].

	Mean shape of SSM	Mandible used in this thesis	SSM Vallabh [8] F/M
Intercondylar distance [mm]	110,71	118,18	114,8 / 120,8
Intergonial distance [mm]	86,44	93,02	86,2 / 95,6
Body width [mm]	10,6	11,05	10,2 / 12
Body length [mm]	76,66	83,35	72,7 / 78,6
Ramus height [mm]	66,39	65,56	61,0 / 69,6
Ramus width [mm]	31,58	29,72	29,8 / 31,7
Condyle height [mm]	20,74	19,02	19,5 / 20,2
Pogonion lateral condyle distance [mm]	120,72	118,52	114,7 / 119,9
Gonial angle [°]	127,69	130,20	128,2 / 121,3
Body height [mm]	30,44	32,31	26,7 / 29,8
Pogonion interdental distance [mm]	26,56	31,07	22,2 / 21,4
Intercondyle angle [°]	132.77	126.21	128,2 / 134,7

For the first four modes, the related morphological measurements were measured for the patients who had the minimum and maximum standard deviations for these modes, to verify that the expected differences occurred. These b-values and the measurements related to the previously mentioned shape variations are reported in table 6. Measurements related to the variations of mode 1 verified the observed variations between the condylar distance and angle, within mode 2 only the gonial angle largely differed between the mandibles with maximum and minimum standard deviations. Smaller differences were seen in the measurements of the maximum and minimum standard deviations of mode 3 and 4, however they still verified the observed variations reported previously.

Table 6: Mandibular morphometric measurements that are associated with the first 4 modes of the SSM for the cases with max standard deviations (i.e. the minimum and maximum b-values).

Mode	Measurement	Case min std.dev	Case max. std.dv
1	Intercondylar distance [mm]	80	88
	Intercondylar angle [°]	142	88
	Ramus Length [mm]	67	48
	Body Length [mm]	88	57
	Pogonion-interdental distance [mm]	35	26
2	Gonial angle [°]	127	107
(-1.89 → +2.04)	Body width [mm]	24	25
	Ramus width [mm]	23	27
	Pogonion-interdental distance [mm]	31	33
3	Condyle length [mm]	17	15
(-1.79 →+1.97)	Ramus width [mm]	29	33
4	Process length [mm]	32	36

3.3 IMPLANT DESIGN

All four manually adapted models, which visualized the four defect scenarios, were used to estimate the missing bone shape, using three different methods. This estimated shape was then used as a base for reconstruction implants. Firstly, an automatic extruded base option in 3-matics for missing anatomy, in which only the two contours of the remaining bone needed to be selected, was used. Secondly, the SSM was used to estimate the missing bone part. And thirdly, mirroring of the intact side of the mandible was used, using the midplane of the mandible as mirroring plane. Results are illustrated in figure 13, in which extruded base, SSM and mirroring are represented as orange, pink and blue implants, respectively. In case of the symphysis defect, the mirroring technique is not available since the intact side was affected too. For the estimation of the missing part using SSM, a MATLAB code was used to match the remaining bone with the SSM made prior. The STL-file outputted was of the newly generated full mandible. However, the quality of the surface of the STL was rough. Alignment of this estimated full mandible shape with the remaining bone was therefore difficult, and manually alignment did not result in an appropriate implant design after cutting the new estimated missing part out of the full estimated mandible. However, this study merely showed the possibility of using a SSM and future studies will use an improved MATLAB code. In table 7 the volume and surface of the removed part of the bone and all created implants' bases are reported. Which shows that the SSM and mirroring often have similar volume and surface as the missing part. Extruded base volume and surface however, were smaller with 50% defect scenarios, since anatomical futures like the coronoid process and gonial angle were not taken into account.

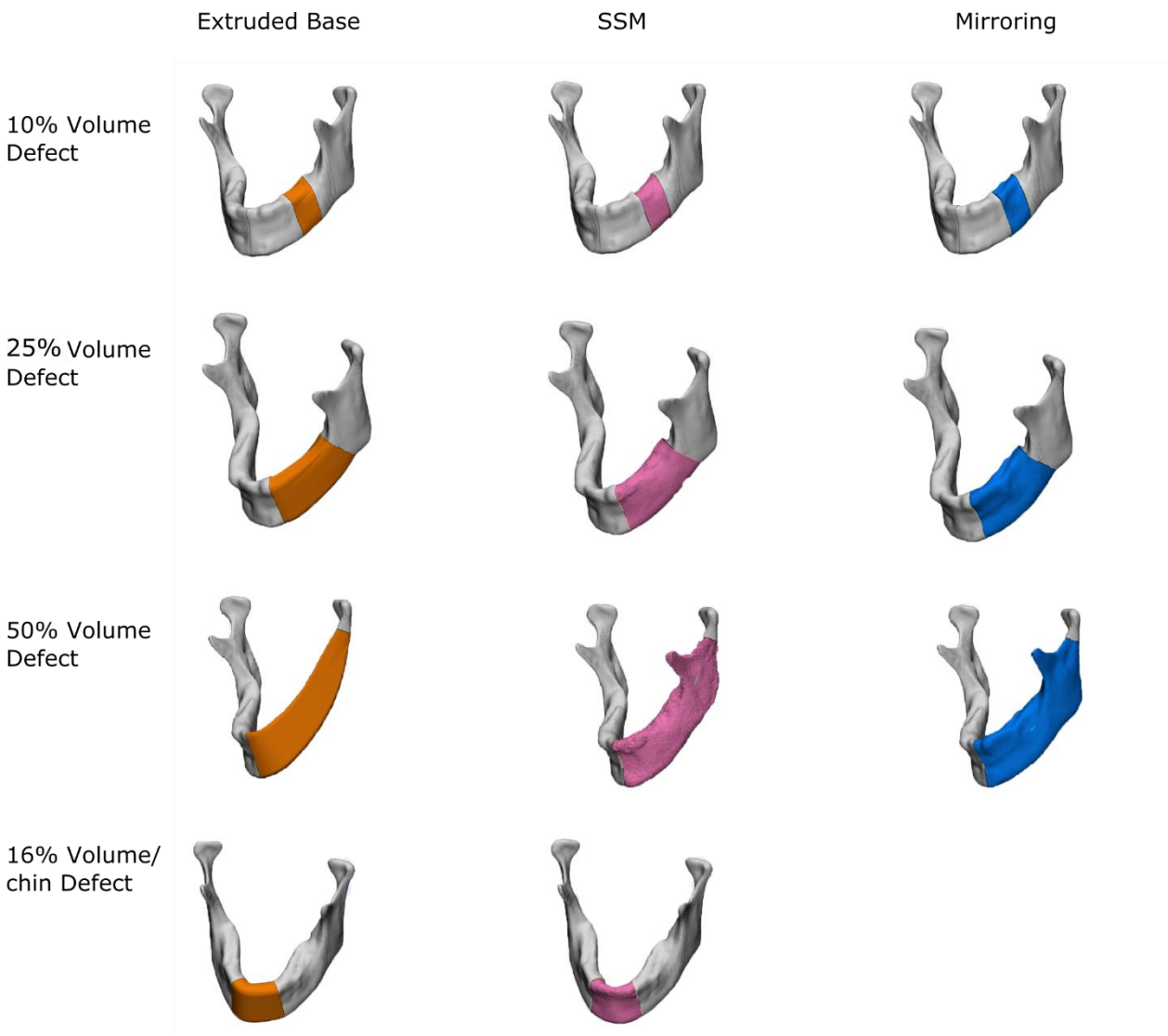

Figure 13: Results for all four defect scenarios using three different methods; extruded base (orange, left) SSM (pink, middle) and mirroring of the healthy side (blue, right).

Table 7: Volume and surface of the missing part and the implants created with three different techniques, extruded base, SSM and mirroring of the healthy side for four different defects on the mean mandible.

		Volume [mm²]	Surface [mm²]
10%	Missing part bone	7358	2389
	Extruded base	7461	2356
	SSM	7484	2365
	Mirroring	7282	2365
16%	Missing part bone	11847	3520
	Extruded base	13952	3607
	SSM	11942	3544
	Mirroring	-	-
25%	Missing part bone	17999	4830
	Extruded base	19252	4848
	SSM	18074	4653
	Mirroring	18401	5009
50%	Missing part bone	34519	9717
	Extruded base	26557	7290
	SSM	33425	8965
	Mirroring	31665	9341

The point cloud from the originally missing anatomy (*i.e.* the manually removed part) was compared to the estimated shapes created with the three methods using Cloud Compare (open software, [21]). The maximum and average distances between this originally missing part and the point cloud of that of the created implant were calculated for all four defect scenarios and repeated for four additional mandibles. Results are reported in figure 14 and 15 as a mean of the total 5 mandibles and the standard deviations are reported with the error bar. Maximum differences for SSM and mirroring methods were often found close to the attachment to bone, due to improper alignment (see 25% volume defect in figure 13). For the extruded base these maximum differences were found near the gonial angle and coronoid process, since those were not present in the estimated shape with extruded base. Significant differences were found in maximum distances between the extruded base and SSM methods for the 16% volume defect ($p=0.013$), the extruded base and SSM methods for the 50% volume defect ($p=0.007$), and for the extruded base and mirroring methods for 50% volume defect ($p=0.0$). Between the other maximum distances for each defect scenarios, no significant differences were found. Significant difference was only found in average distance between the extruded base and SSM methods for the 16% volume defect ($p=0.007$). Between the other average distance for each defect scenarios, no significant differences were found.

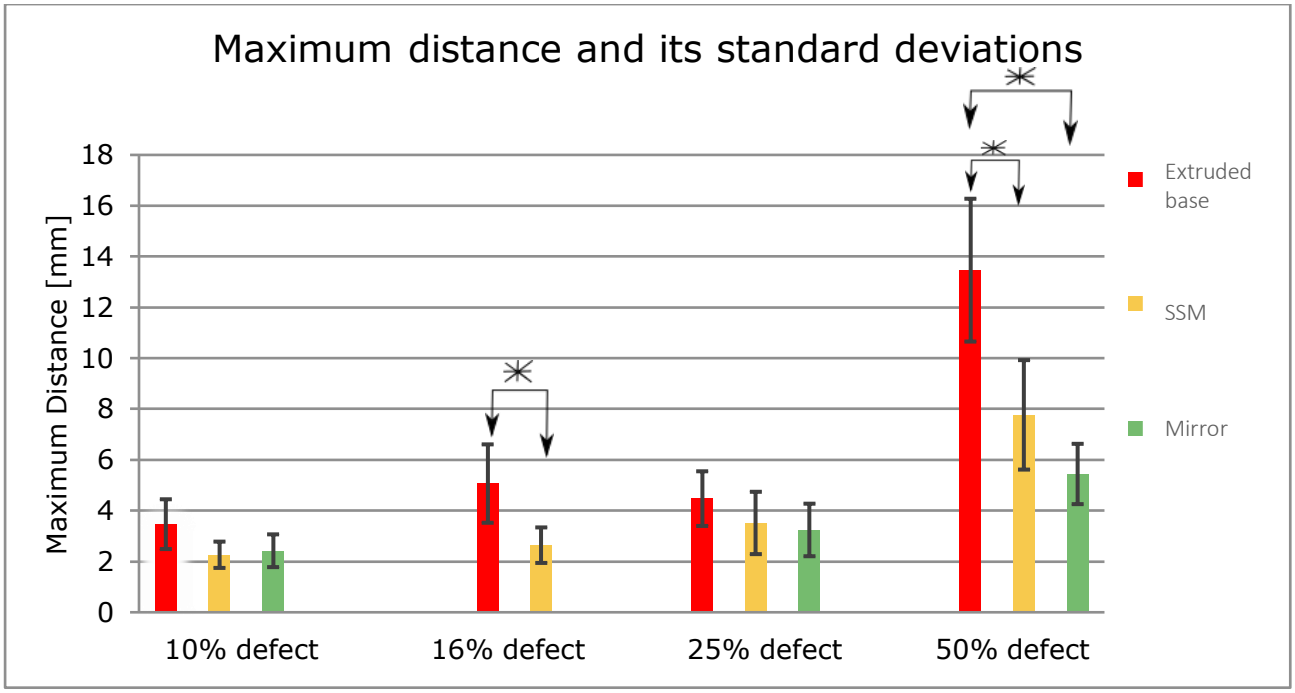

Figure 14: Graph showing the mean errors as maximum distance [mm] between pointclouds of implant design and missing part for all four defects using three different techniques; extruded bases (red), SSM (yellow) and mirroring (green). A total of five patients were included. Statistical significance is illustrated with a star (✳).

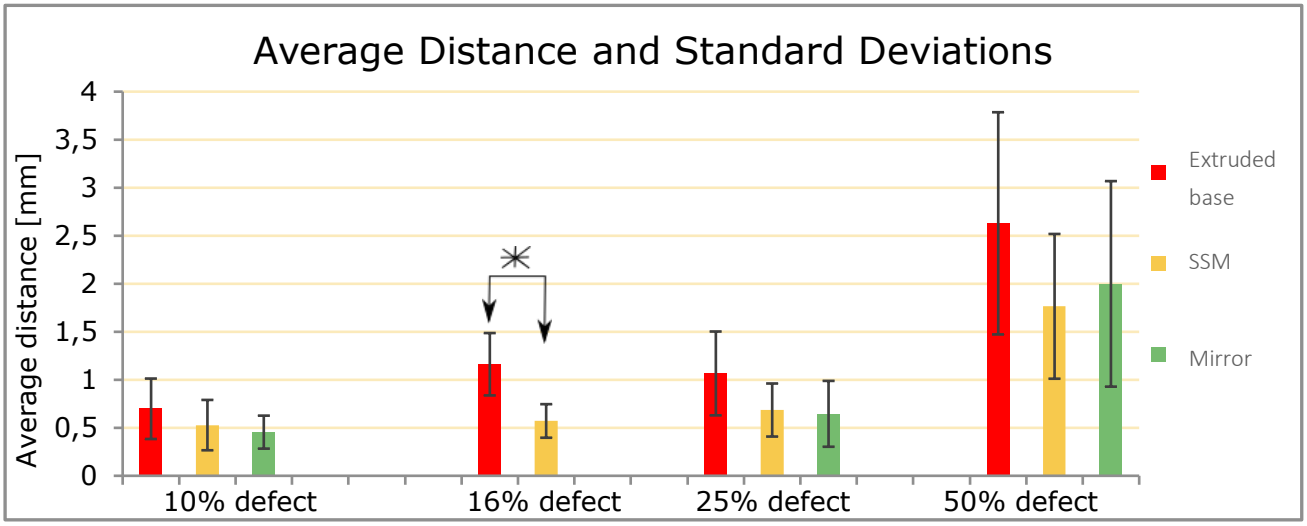

Figure 15: Graph showing the average distance[mm] between pointclouds of implant design and missing part for all four defects using three different techniques; extruded bases (red), SSM (yellow) and mirroring (blue). A total of five patients were include. Statistical significance is illustrated with a star (✳).

To investigate if the use of SSM was superior to other simpler methods, benefits and limitations of all three methods were investigated. Benefits of the extruded base model included simplicity, since only the outer contours of the remaining bone parts needed to be selected. However, limitations included large errors when defect size increased (figure 14, 15), loss of both anatomical landmarks and overall shape, since the curvature of the mandible had to be estimated. Benefits of the mirroring technique includes simplicity as well; no additional database is needed. For maximum and average distances no statistical significance was found ($p \geq 0.05$) for the five cases between the mirroring and SSM methods. However, since asymmetry takes place in the mandible in mainly the rami, body and condyles [29, 30], mirroring of the mandible is often impossible. A previous study [31] states that this technique cannot duplicate a mandible completely and limits the use of this technique. Manual alignment of the mirrored side was subjective and challenging, and some defect scenarios cannot be treated with this technique, since a healthy side needs to be present. Therefore, symphysis cases cannot be treated (figure 13, 14, 15) as well as cases in which the trauma is so severe that both sides are affected. Finally, the use of SSM, which was independent of the size and location of the defect and anatomical landmarks were reproduced as well. Although a relatively big database needs to be created of healthy mandibles, the final use was rather easy and straight forward. In the case of an implant, almost all defects could be managed. In this study even defects up until 50% showed promising results. The graphs (figure 14 and 15) reported similar results as the mirroring method. However, since the code used is not optimized yet, the results in this case were merely a proof of concept. It is suggested that final improvements will decrease the distances more.

The SSM implant needed manual adaptations for proper alignment with the remaining bone. These final steps were taken in 3-Matic (Materialize, Belgium), using the push and pull options and local smoothing of the surface. The manually adapted implant is shown in figure 16 and had a volume of 18074 mm^3 and a surface of 4653 mm^2.

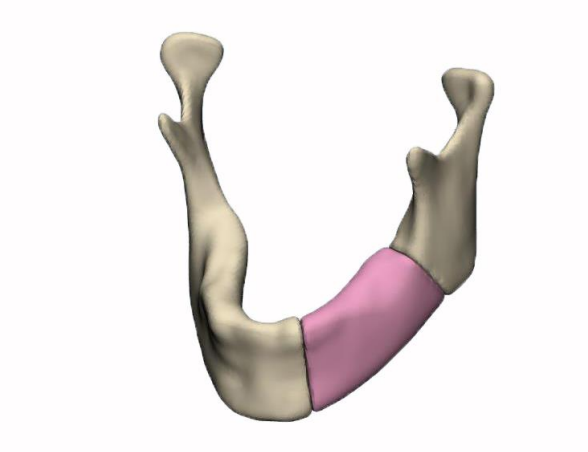

Figure 16: Manually adapted solid implant for a 25% total volume defect located at the mandibular body, shape obtained using SSM.

3.4 FINITE ELEMENT MODELLING

3.4.1 Incision Clenching Loading Condition

The stress and displacement were first calculated on the healthy fully intact mandible. It was compared to literature to investigate if similar stress concentrations and displacement patterns were obtained. This helped verify the loading conditions. Additionally, the results of this FEM were compared to the optimized implant, to check if maintenance of the stress and displacement distribution of the mandible occurs.

The von Mises stresses results of the FEM under INC loading for the healthy intact mandible and the mandible including the solid implant are shown (figure 17 and figure 18, respectively). For the healthy mandible, the maximum stress was measured to be 1722 MPa, however this is only at the incision bite constraint. Lower stress concentrations of around 40Pa were present around the posterior side of the ramus, the alveolar, as well as at the condylar neck.

The mandible with the solid titanium implant (figure 17) had a maximum von Mises Stress of 787 MPa, located at the incision bite constraint area too. In the rest of the mandibular bone, higher stress concentrations were located at the posterior border of the ramus, as well as at the alveolar region. The implant had higher stress concentrations on the lateral superior side of the posterior ending and at the lateral inferior side of the anterior ending.

Displacements for both models are represented in figure 19 and figure 20, in which the undeformed mesh is illustrated in grey. The healthy mandible (figure 19) had a maximal displacement of 3.05 mm to the anterior left side of the mandible. The mandible body and ramus moved mainly in the forward/anterior direction, but the ramus also moved slightly in the upwards/superior direction. The coronoid processes move slightly inwards.

The mandible including the solid implant (figure 20) had a maximal displacement of 2.88 mm at the anterior lateral right side of the mandible. The mandible also moved forward and slightly upwards with the implant. There was a slight inward displacement of the coronoid processes as well. However, displacement of the mandible was superior to the right lateral side.

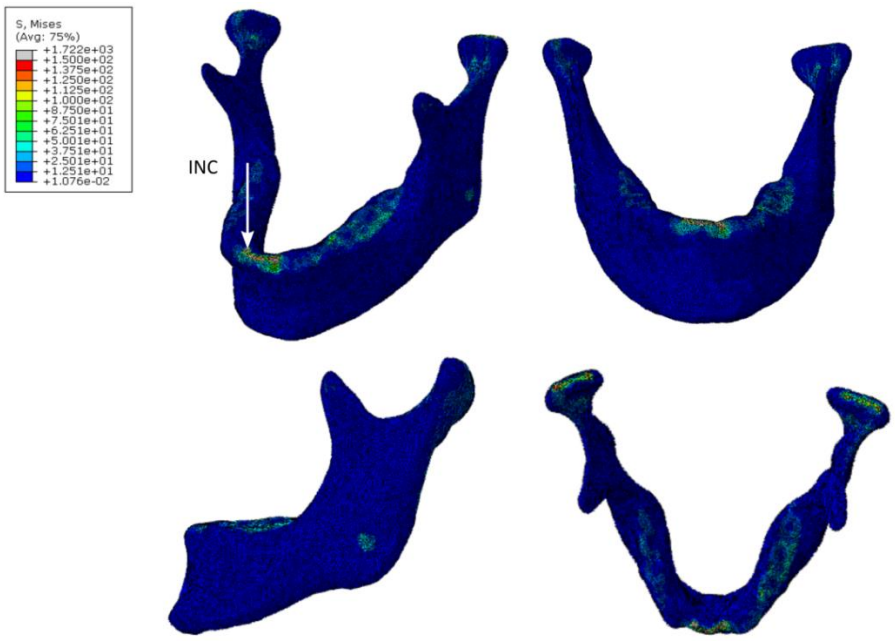

Figure 17: FEM results for von Mises stresses [MPa] for the INC of a healthy mandible in isotropic (top left), posterior (top right), superior (lower left) and cross section (lower right) view.

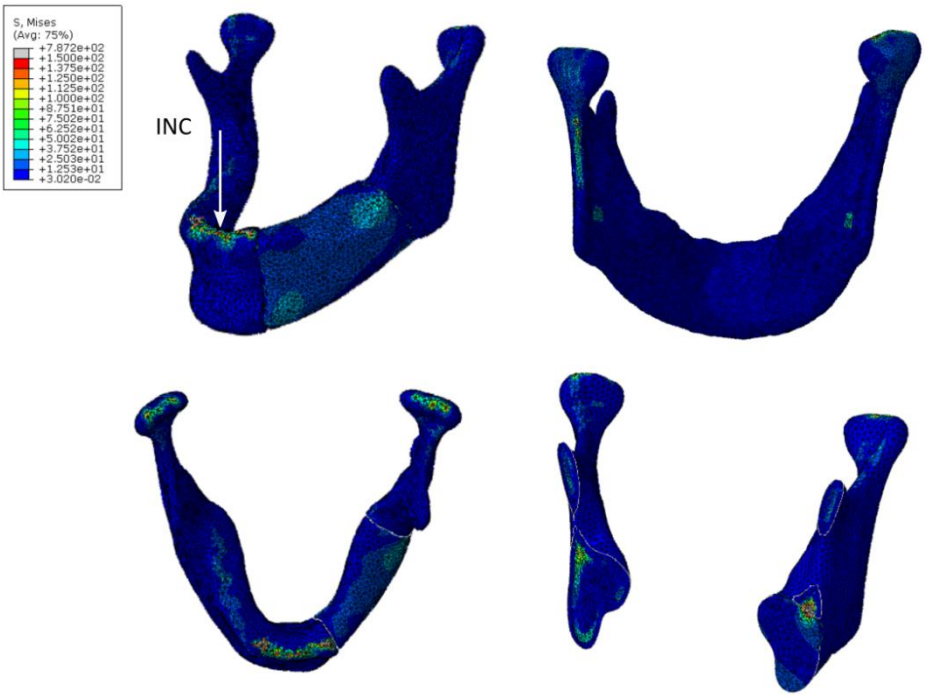

Figure 18: FEM results for von Mises stresses [MPa] of a mandible with 25% volume defect and a solid titanium implant in isotropic (top left), posterior (top right), superior (lower left) and cross section (lower right) view.

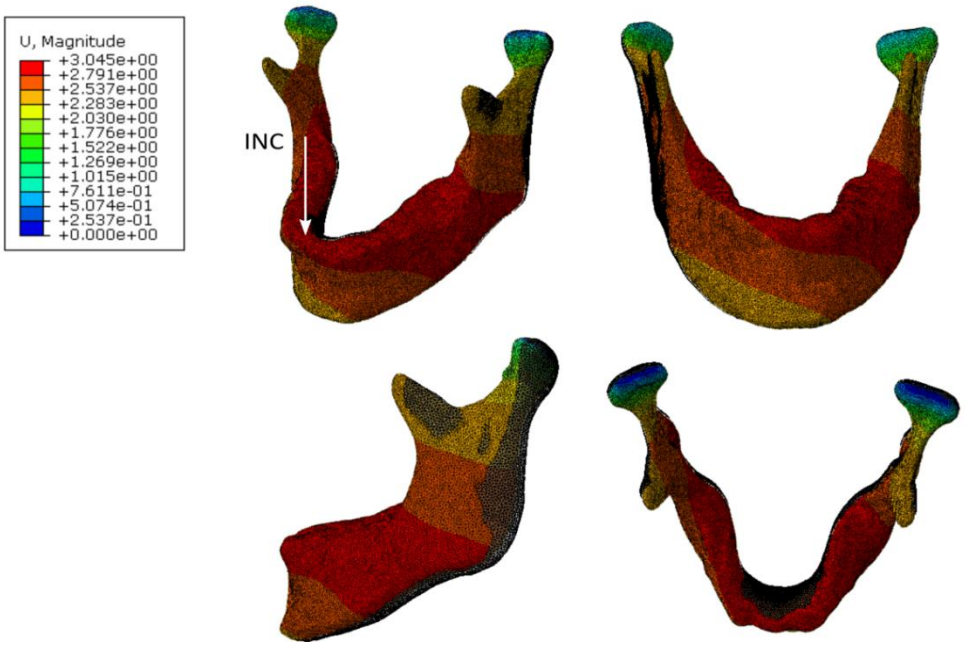

Figure 19: FEM results for displacement [mm] of the healthy mandible in isotropic, anterior, left lateral and superior view. Undeformed shape is illustrated in grey

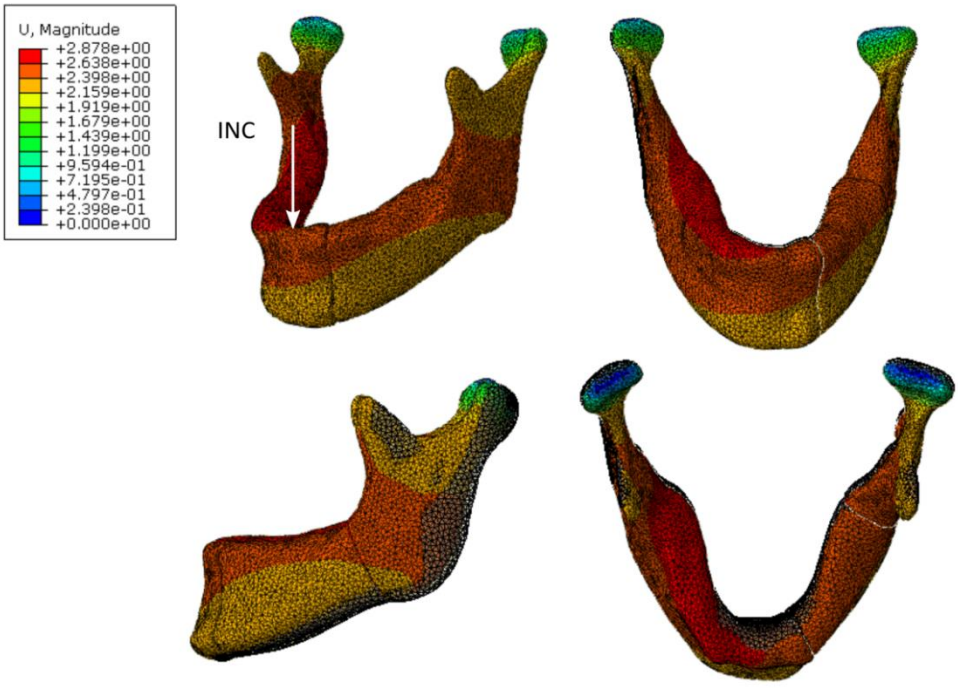

Figure 20: FEM results for displacement [mm] of the mandible with 25% volume defect and a solid titanium implant in isotropic, anterior, superior and left lateral view. Undeformed mesh is illustrated in grey.

3.4.2 Right Molar Biting Loading Condition

The von Mises stresses and displacements results of the FEM under RBM loading for the healthy complete mandible and the mandible including the solid implant are shown in figure

21 and figure 22, respectively. The highest von Mises stress in the healthy mandible was measured at the incision area, the molar on the right side, to be 490 MPa. However, also the molar section on the left side was affected. The left lateral side showed a small stress concentration. Maximum displacement occurred on the left lateral side, around the gonial angle and reached 1.187 mm. The mandible moved slightly forward/anterior and the left side moved in medial/inward direction.

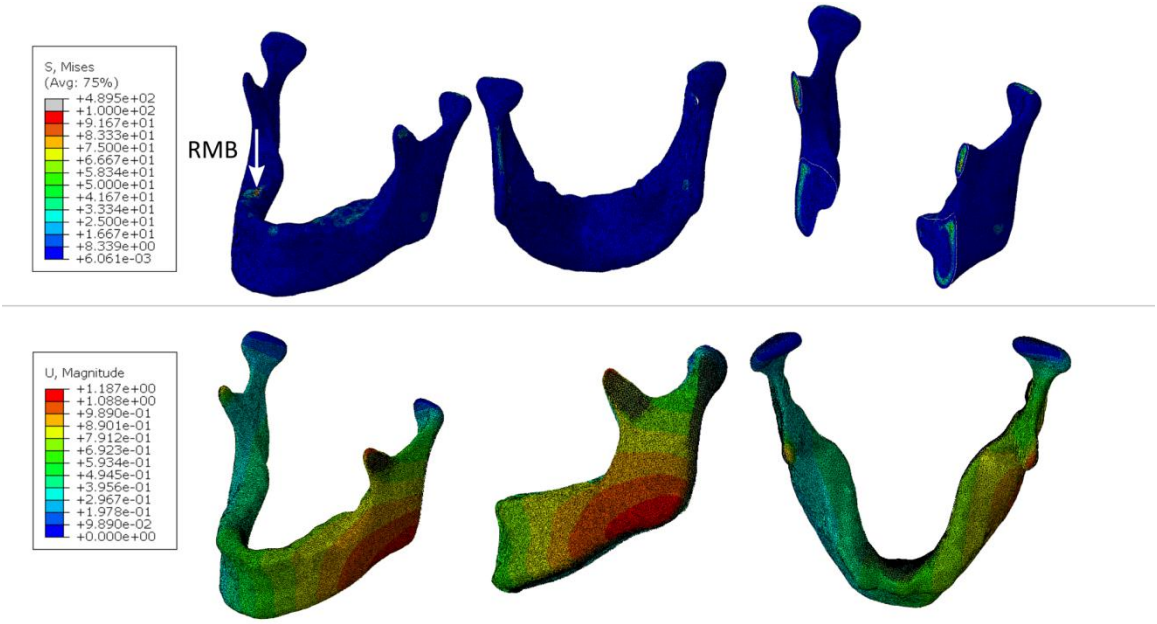

Figure 21: FEM results for both von Mises stresses [MPa] (top, in isotropic, posterior, and in cross section view) and displacement [mm] (bottom in isotropic, left lateral, superior and left lateral view) for the RMB task.

The model including the implant (figure 22) reached the highest von Mises stress of 406 MPa at the incision area as well. Stress concentrations within the implant were found at the left posterior superior side. Maximum displacement occurred at the left side, mainly around the gonial angle, of around 1.058 mm. Other high deformations occurred at the end of the left coronoid process.

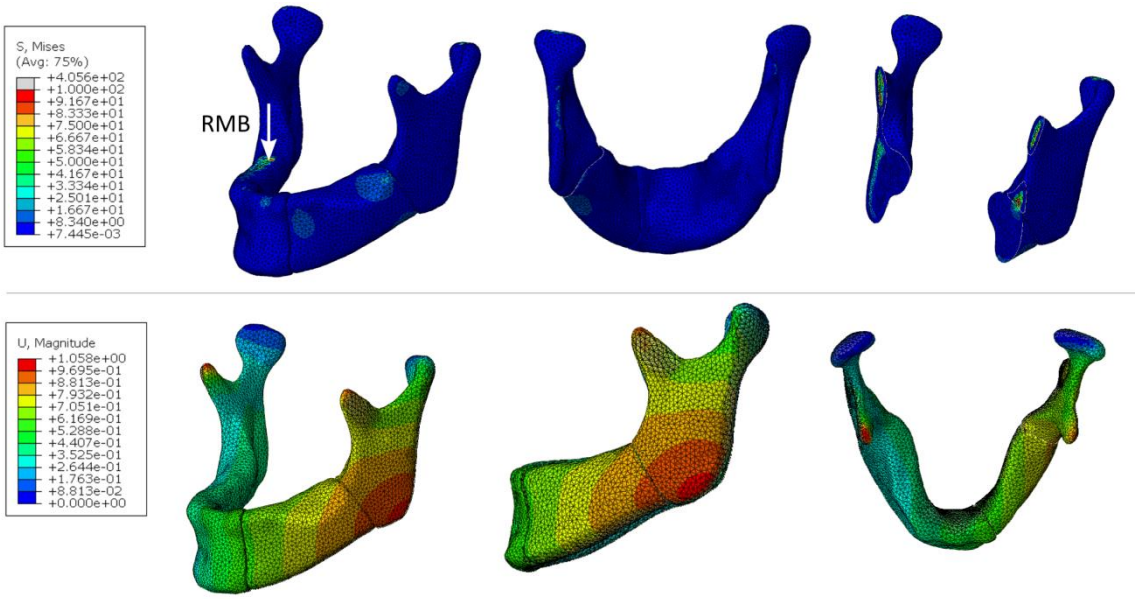

Figure 22: FEM results for both von Mises stresses [MPa] (top, in isotropic, posterior, and in cross section view) and displacement [mm] (bottom in isotropic, left lateral, superior and left lateral view) for the RMB task.

3.5 TOPOLOGY OPTIMIZATION

3.5.1 Topology Optimization Mean Model Outcomes

In figure 23, three graphs of the topology optimization process are shown. These illustrate the objective function (*i.e.* minimalize SE) in red and the constraint function (*i.e.* volume) in blue with respect to the amount of cycles that were needed for the simulation. The three graphs from left to right are for the topology optimization for INC with volume constraint 0.2, for INC with volume constraint 0.24 and for RMB with volume constraint 0.2, respectively. The strain energy in the graphs started to stabilize around 15 cycles, and completion of the topology optimization was before the defined maximum number of 35 cycles. The topology optimization under INC loading conditions needed 28 cycles, those under RMB loading conditions 25 cycles.

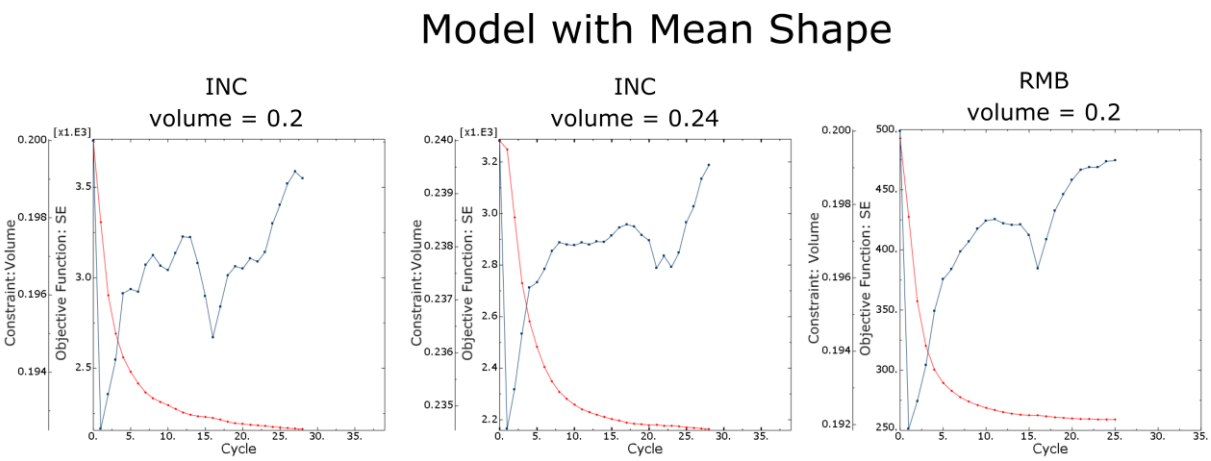

Figure 23: Graphs showing the object function of minimalizing the Strain Energy (SE) (red line) and the constraint of volume (blue line) for all three topology optimizations of the model with the mean shape.

Results of the topology optimization are shown in figure 24, 25 and 26 for two volume constraints of 0.2 and 0.24 for INC and the volume constraint 0.2 for RMB, respectively. Shown in these figures are the final mesh calculated for the last cycle, the maximum von Mises stress distribution and the displacements both in anterior and isotropic view.

The implants created under INC loading conditions (figure 24 and 25) had their maximum von Mises stresses at the incision bite boundary constraint. However, von Mises stresses of around 300 MPa were measured within the implants. High stress concentration occurred at the superior border of the implant and inferior right lateral crossing for both implants generated under INC loading conditions (*i.e.* with 0.2 and 0.24 volume constraint). In the implant with the 0.2 volume constraint, extra stress concentrations occurred at the posterior superior border with the ramus. Maximum displacements under INC are similar; 3.076 mm and 3.056mm and located at the anterior left lateral side of the mandible. Displacements were both forwards and slightly upwards.

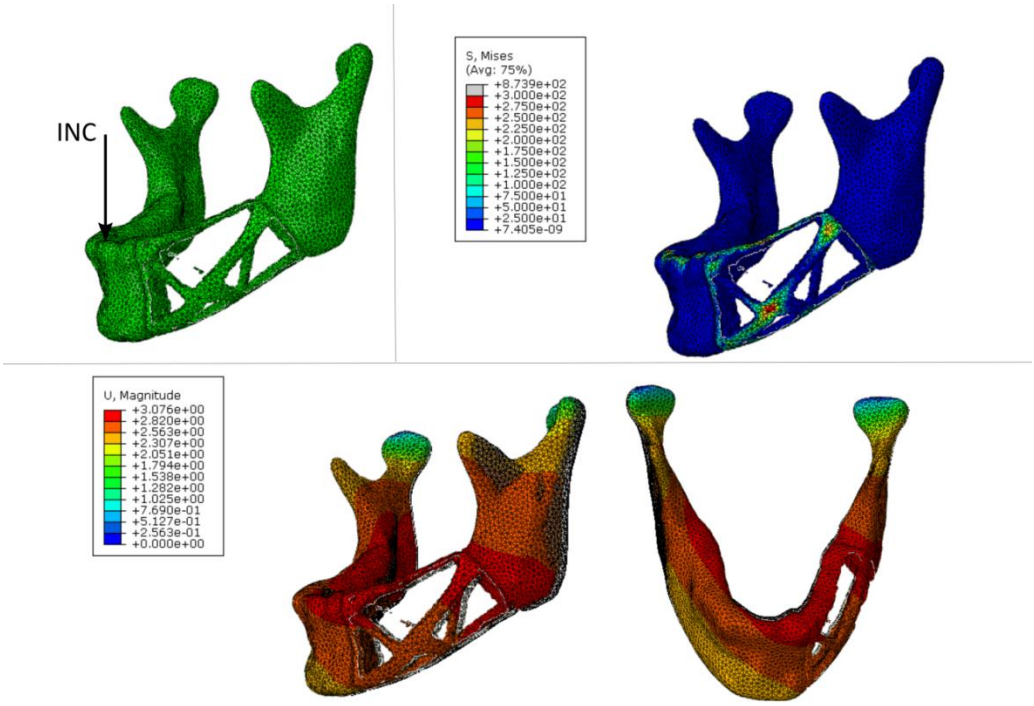

Figure 24: FEM results of the topology optimization task under INC loading conditions with volume constraint ≤ 0.20 of original volume. Outcomes are in final mesh (top left), von Mises Stress [MPa] (top right) and displacement [mm] (bottom).

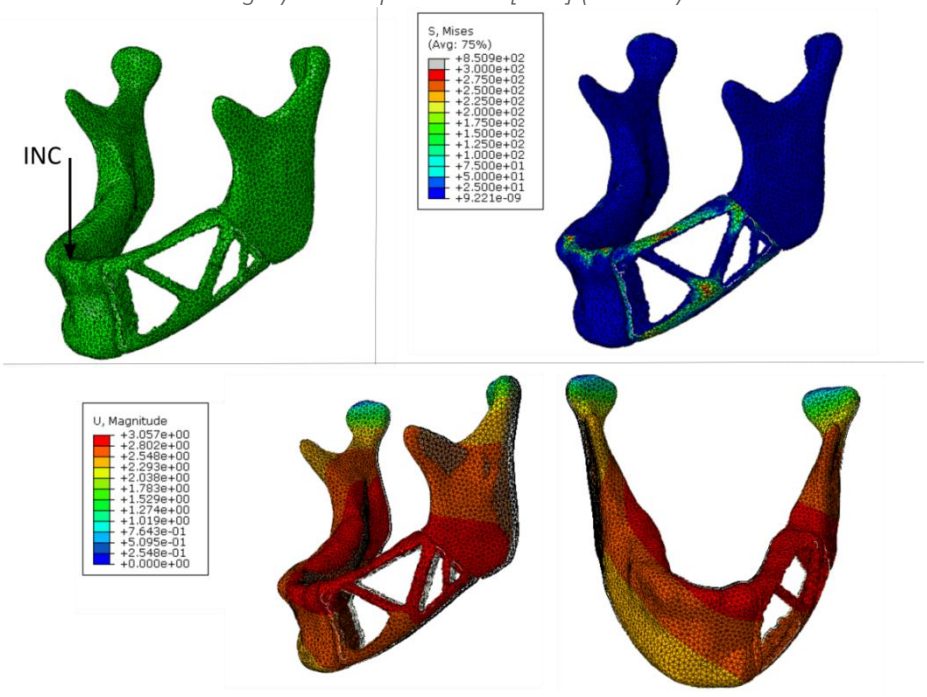

Figure 25: FEM results of the topology optimization task under INC loading condition with volume constraint ≤ 0.24 of original volume. Outcomes are in final mesh (top left), von Mises Stress[MPa] (top right) and displacement [mm](bottom)

The same model was then optimized under different biting conditions, RMB (figure 26). Maximum stresses within the implant was lower and around 110 MPa. Higher strain

concentrations still occurred at the lateral inferior border of the implant, resulting in crossings that were similar in orientations to those orientations of the implant created under INC. Maximum displacement however, occurred at the left gonial angle and left coronoid process and had a value of 1.370 mm.

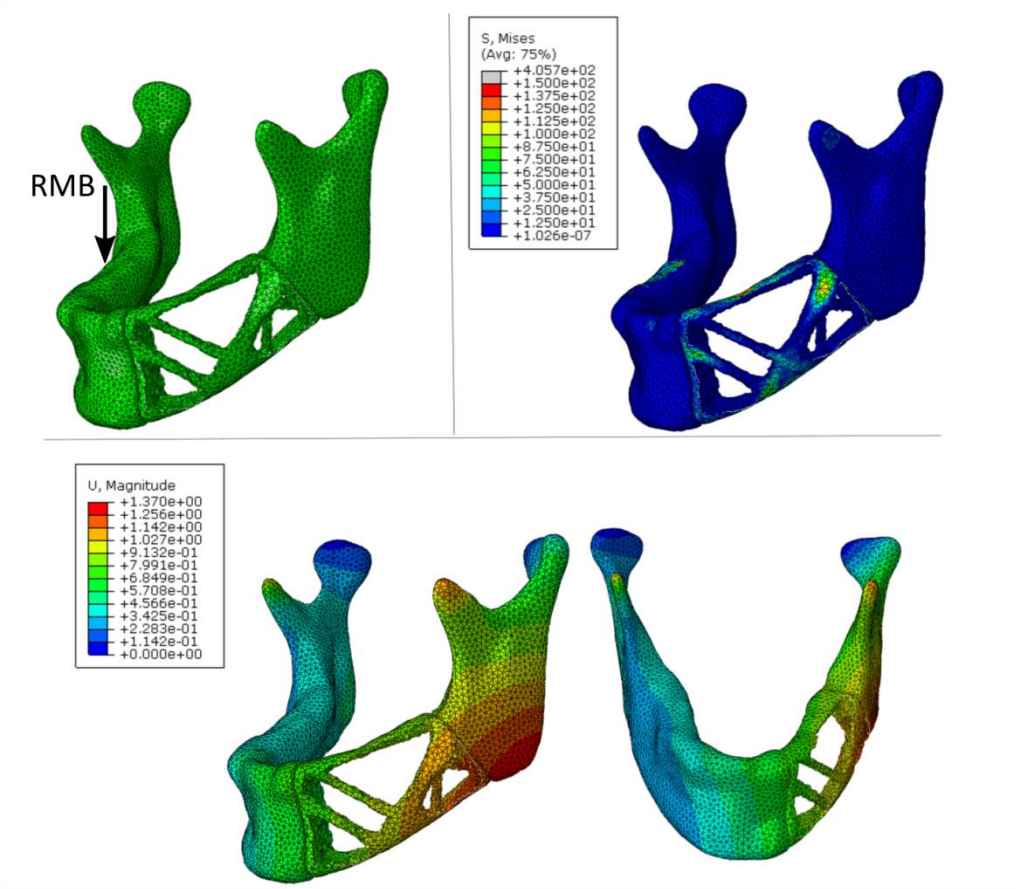

Figure 26: FEM results of the topology optimization task for RMB with volume constraint ≤ 0.20 of original volume. Outcomes are in final mesh (top left), von Mises Stress [MPa] (top right) and displacement [mm] (bottom)

3.5.2 Implant Designs

All of the three topology optimized implants above were manually modified using 3-matic version 13.0 (Materialise, Leuven, Belgium) for smoothing of the rough surface created due to the relatively large element size within ABAQUS. Results of these finalized implants are shown in figure 27 to 29, including one illustration in which the implants are shown with the original missing bone part as a reference. This showed that contours of the final design could follow those of the removed part of the bone. All implants had the created topology optimized frame at the lateral side of the implant, leaving the implant open and hollow at the medial side. Both implants generated under the INC are shown together in figure 30 including some measurements, illustrating that the changes that occur between them are small. Slight

differences were seen at the crossings. The implant with INC and 0.20 volume constraint had a gap between the most inferior border of the implant and its crossing. In the implant with INC and 0.24 volume constraint, this was closed.

Using topology optimization with volume constraint 0.2 with the RMB loading conditions resulted in a slightly different optimized pattern compared to the INC loading conditions. Both implants are shown together in figure 31 including measurements, illustrating that the changes that occur between them are small. The implant with RMB and 0.2 volume constraint has a crossing more anteriorly.

After all the modifications, the final volume of the implant with INC and 0.2 volume constraint was around 4608 mm^3, resulting in a 20.4 grams Ti-alloy implant. For implant with INC and 0.24 volume constraint, the final volume was 5350 mm^3, resulting in a weight of 23.7 grams. The implant with RMB and 0.2 volume constraint had a final volume of 4769 mm^3, resulting in a weight of 21.1 gram. The original weight of the bone that was removed was 19.9 grams, calculated from the density values from the CT data using Mimics.

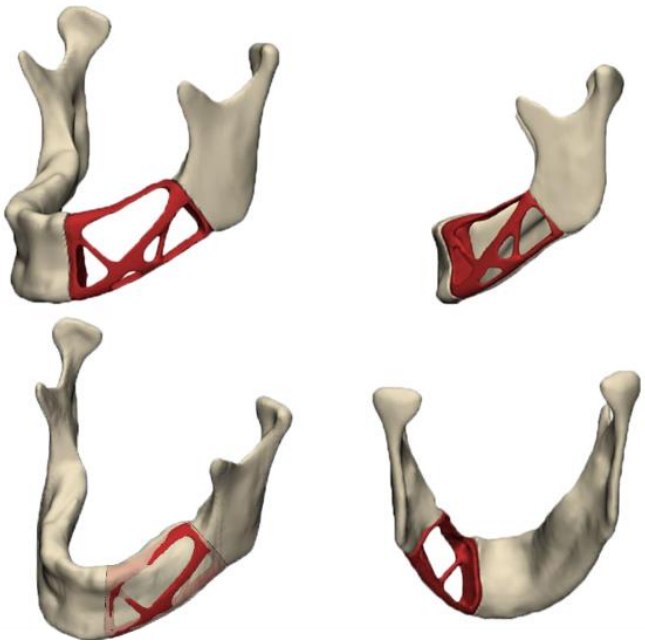

Figure 27: Model with modified implant for INC with the volume constraint of 0.2 and modified. Lower left image illustrates the implant with the original missing bone part as reference.

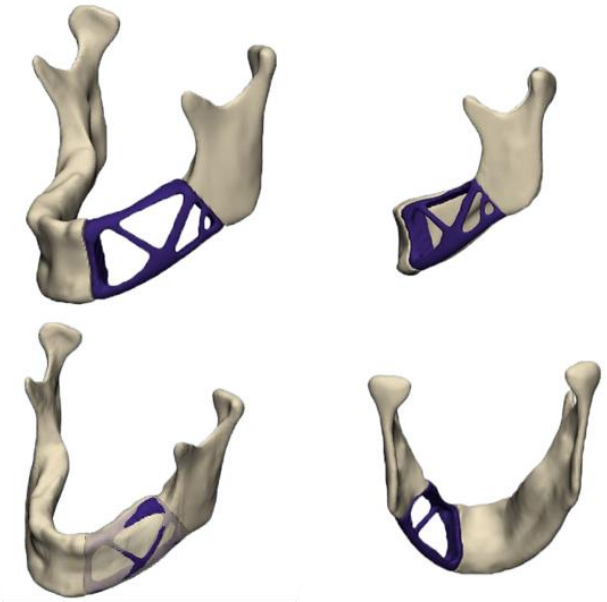

Figure 28: Model with modified implant for INC with the volume constraint of 0.2 and modified. Lower left image illustrates the implant with the original missing bone part as reference.

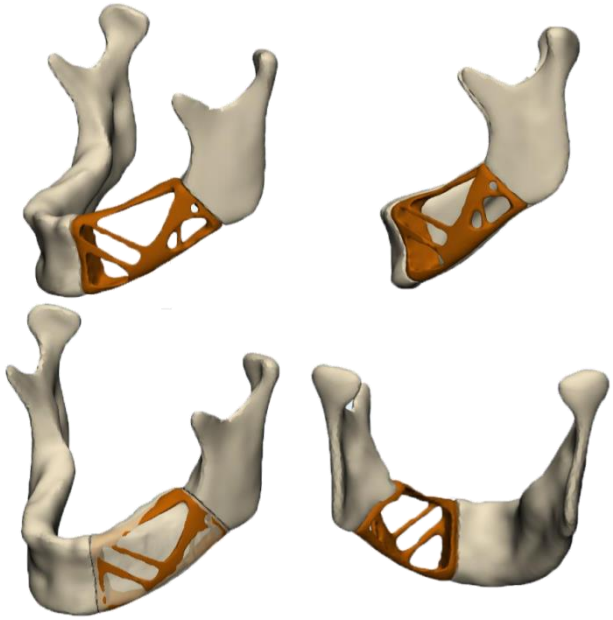

Figure 29: Model with modified for RMB with the volume constraint of 0.2 and modified. Lower left image illustrates the implant with the original missing bone part as reference.

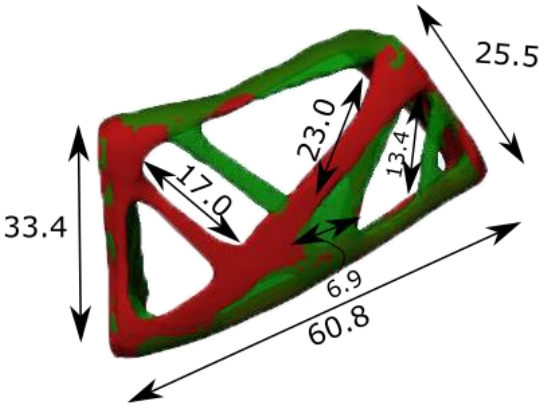

Figure 30: Comparison of modified implants created under INC with different volume constraints of ≤ 0.2 (blue) and ≤ 0.24 (green) with several measurements.

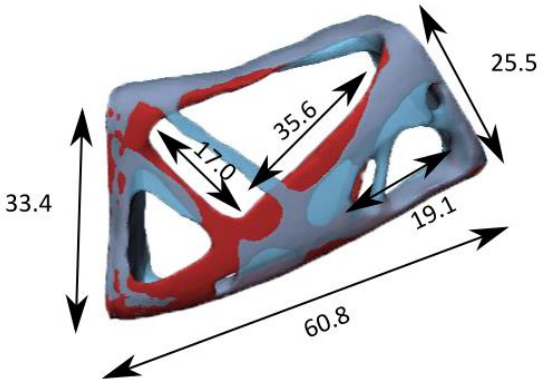

Figure 31: Comparison of modified implants created under INC (red) and RMB (blue) with several measurements.

3.5.3 Stress Comparison Topology Optimized Designs

For the following steps only the implants with 0.2 volume constraint were used. The remodeled implant created under INC (figure 26) was imported to ABAQUS version 2017 (Dassault systems, Vélizy-villacoublay, France) again and new a FEM was made under the RMB loading condition (figure 32). The mesh of the TI_INC contained 8593 elements with a maximum triangle length of 2.0 mm. Results from this are reported as TI_INC_RMB. Maximum von Mises stresses within the implant occurred at the crossings, and were around 120 MPa. The highest von Mises stresses were found in the bone to be 553 MPa. The largest displacement occurred at the left gonial angle and was 1.467 mm.

The remodeled implant created with RMB was also reimported and new a FEM was made under INC loading conditions (figure 33). The mesh of the TI_RMB contained 9059 elements with a maximum triangle length of 2.0 mm. These results are reported as TI_RMB_INC. Von Mises stresses in the implant exceeded 450 MPa and the maximum von Mises stress in

mandible was 2425 MPa, located at the posterior border of the implant with the bone. Maximum displacement occurred between posterior border of the implant and bone and was 5.202 mm.

The average and highest stresses were measured at 3 regions within the bone. These regions were taken as a slice of the condyle neck, a slice of the coronoid process and a section from the gonial angle. Results for the average von Mises Stresses measured are shown in the graphs of figure 34 and maximum von Mises stresses are reported in table 8.

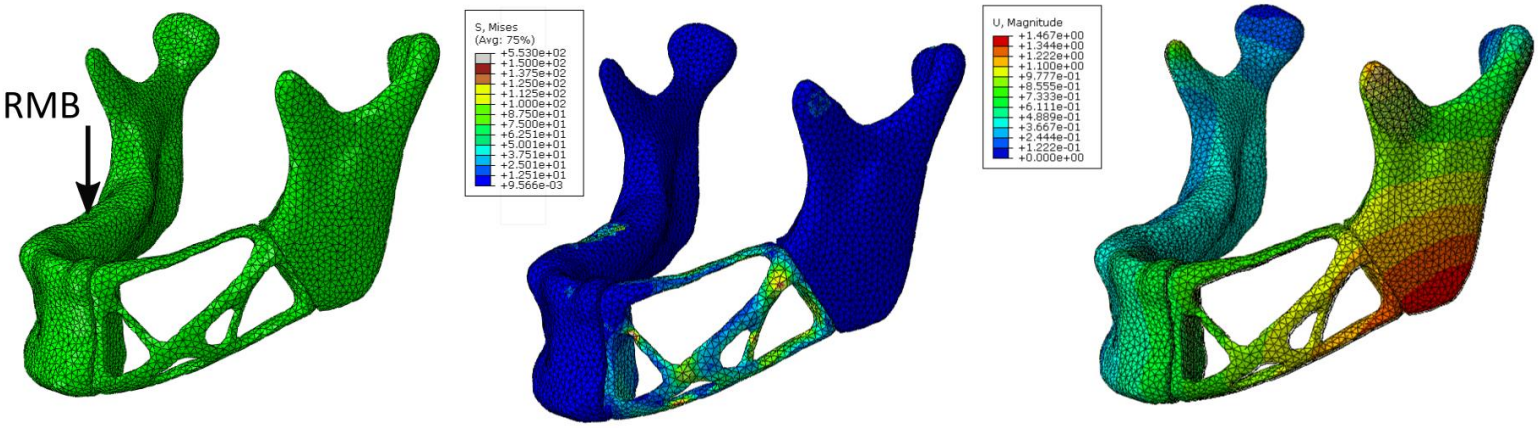

Figure 32: FEM results of RBM of the mandible with the implant created under INC (TI_INC_RMB) for RMB with volume constraint ≤ 0.20 of the original volume. Illustrated are the input mesh (left), von Mises Stress [MPa] (middle) and displacement [mm] (right)

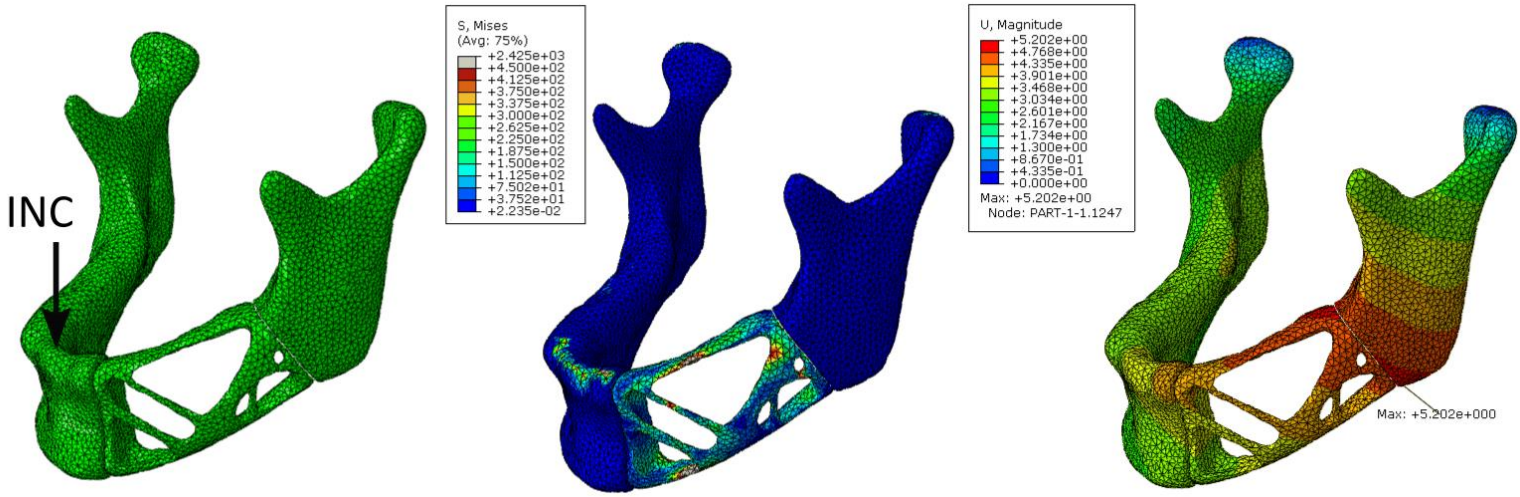

Figure 33: FEM results of INC of the mandible with the implant created under RMB (TI_RMB_INC) for RMB with volume constraint ≤ 0.20 of the original volume. Illustrated are the input mesh (left), Von Mises Stress [MPa] (middle) and displacement [mm] (right)

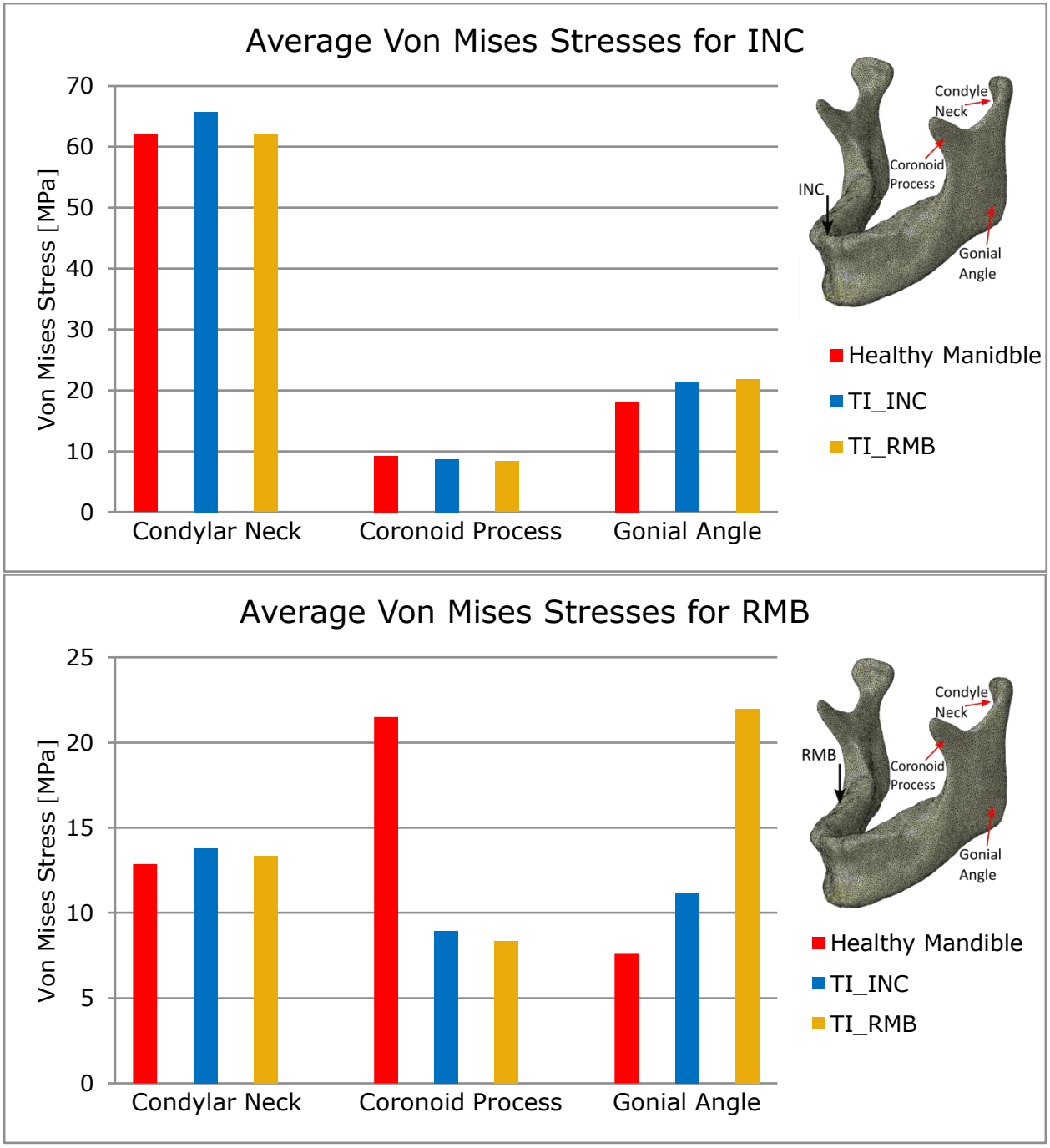

Figure 34: Graphs of the average von Mises stresses taken at sections at three locations; the condyle neck, coronoid process and gonial angle for both the INC loading condition (top) and the RMB loading condition (bottom). Measurements were taken for three models; the healthy mandible, the mandible including the final implant created under INC (TI_INC) and the mandible including the final implant created under RMB (TI_RMB).

Table 8: Maximum von Mises stress measured at three sections of the mandible on the healthy intact mandible, the TI_INC and he TI_RMB for INC and RMB.

	INC			RMB		
	Healthy Mandible	TI_INC	TI_RMB	Healthy Mandible	TI_INC	TI_RMB
CONDYLAR NECK	298,9	315,4	279,83	66,3	63,28	68,3
CORONOID PROCESS	52,92	44,52	41,17	129,56	44,86	34,28
GONIAL ANGLE	167,47	79,87	165,05	41,79	68,11	110,3

3.5.4 Topology Optimization Additional Cases

In figure 35 the result for the case where the initial implant was modelled as a porous structure is presented. The graph shows the objective function (*i.e.* minimalize SE) and constraint function (*i.e.* volume ≤ 0.2362) with respect to the amount of cycles needed for the simulation and the optimized mesh. The topology optimization was done under INC and the final frame was mainly located at lateral inferior side of the mandible.

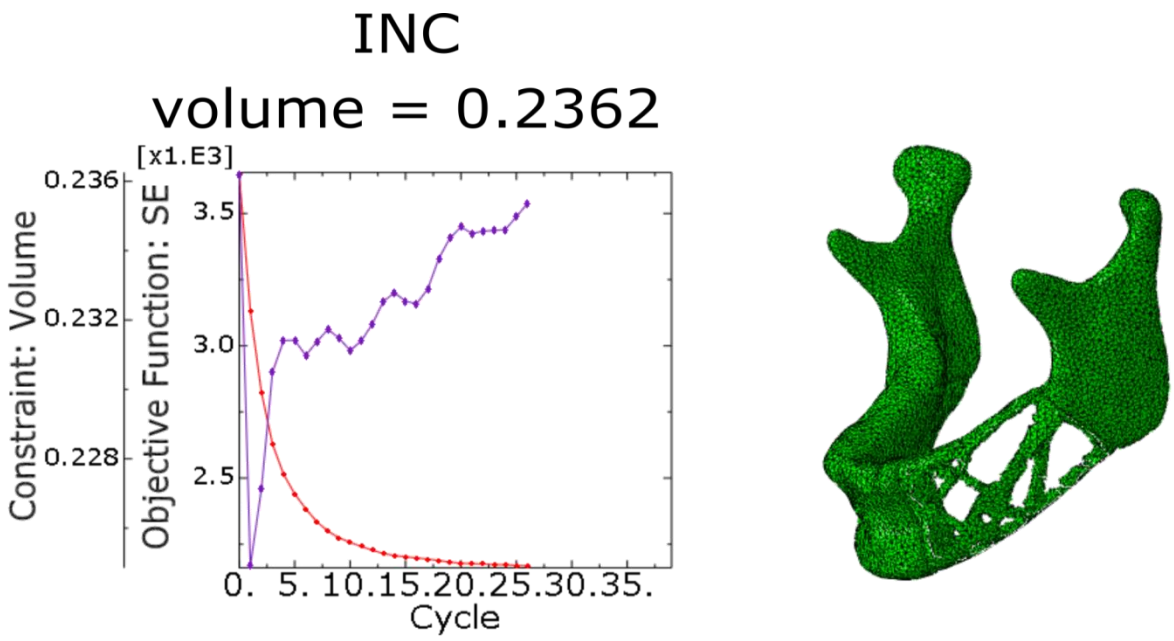

Figure 35: Results of the model in which the initial implant included pores. Graphs (left) with the objective function (red, minimize SE) and constraint (blue, volume ≤ 0.2362 of initial volume) for every cycle that was needed for the topology optimization. Outcomes are given in the mesh (right), representing the newly created shape of the implant.

The mandible bones that varied the most in direction of the first mode were retrieved from the dataset. This mode describes the intercondylar distance and angle, and is related to the

general size of the mandible. Measurements of these mandibles were previously reported (table 6). For the mandible with smallest standard deviation, a total of 66265 and 217870 elements for the solid implant and mandible were used, respectively. The model with the biggest standard deviation included 39981 and 142081 elements for the solid implant and mandible, respectively. For both models a maximum triangle size of 2 mm was used.

Results are presented in graphs with the objective function (*i.e.* minimalize SE) and constraint (*i.e.* volume) over the required cycles and the finalized mesh (figure 36). This illustrated that every mandible had a unique outcome.

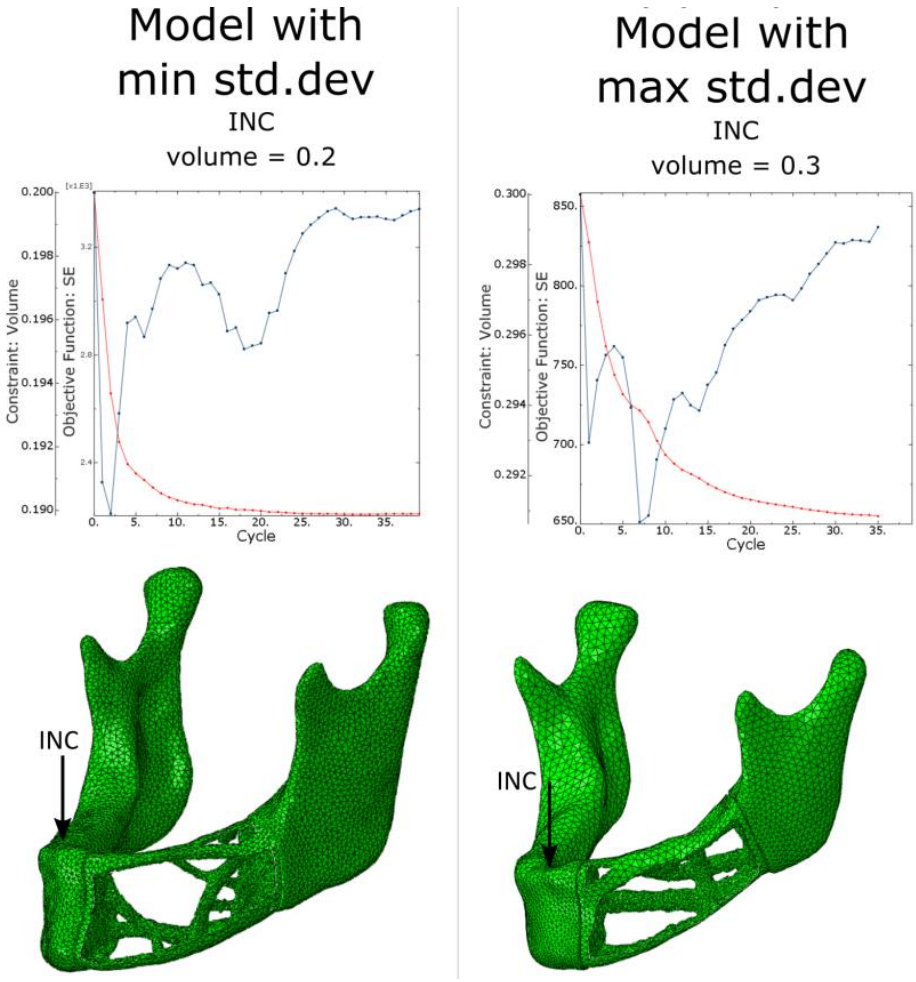

Figure 36: Graphs (top) with the objective function (red, minimize SE) and constraint (blue, volume ≤ 0.2/0.3 of initial volume) for every cycle that was needed for the topology optimization. Outcomes are given in the mesh (bottom), representing the newly created shape of the implant.

3.6 PRINTING DATA

The intact healthy mandible and the mandible with a 25% volume defect with the patient-specific reconstruction implant created by topology optimization under INC loading conditions and a volume constraint of 0.2 were printed using the FDM additive manufacturing process. These are shown in figure 37.

Figure 37: Additively manufactured models of the healthy intact mandible (left) and the mandible with 25% volume defect with the topology optimized implant (right).

4

DISCUSSION

The aim of this thesis study was to use the mandibular bone as a proof of concept to establish a semi-automatic workflow starting from post-processing of computed tomography (CT) scans to the creation of a light-weight additively manufactured patient-specific implant. 35 mandibles were segmented from full-body CT scans to use as the input database. The statistical shape model (SSM) was generated based on these 35 mandible models and proved to work sufficiently well enough for the proof of concept. However, small adaptions needs to take place. Topology optimization for several different cases resulted in unique frames, which can be used as a base for the design of partial mandible reconstruction implants. Every step taken in this thesis will be discussed in the chapter.

4.1 STATISTICAL SHAPE MODEL

The SSM used in this study was created commonly for both male and female mandibular bones. No statistical differences were observed with the b-values generated with this SSM between male and female mandibular shapes. Therefore, there was no need to create gender specific SSMs.

Several SSMs of the mandible have been published in literature [8, 32-36]. Some studies used patches [37], some used only several manually assigned points on anatomical landmarks [34] or some used an eigenfunction of the Laplace-Beltrami operator to obtain the mandibular centerline [36]. Only several use all measurement and volume shapes for reconstruction purpose [8, 32, 33]. In [8] and [33], the first mode was mainly concerned with the general size. However, in the SSM created for this thesis, all mandibles were scaled and translated to the mean shape in the first step. Therefore, size was not illustrated in the modes of variations. Nonetheless, when individual models of the minimum and maximum standard deviations for the first mode were investigated, variations in size were clearly visible. This was verified with measurements from table 6. Other variations that were observed in the published SSM studies similar to this study were width of both body and ramus, shape of the

condyle, pogonion-interdental distance, gonial angle, and ramus height and changes in the coronoid process. The contribution of the first mode was higher in both studies, that is the first mode contributed for 43.46 % [33] and around 32 % and 37 % [8], while in this study the first mode contributed to the overall shape for 24.14 %. This could be explained with the elimination of the general size component.

A limitation of the SSM is the condyle, which was especially evident at maximum standard deviations in the second and third mode (figure 11). An explanation for this could be that the number of points on the condylar section of the mandible is not sufficient enough to describe all variations, since the condyle varies much between mandibles [38]. This is both in shape [39] (*e.g.* flattened, convex, angled or rounded surfaces) and the orientation of the condyle, that is that the condyle can be turned more inwards (*e.g.* the condylar angle changes) [40]. Since the aim of this thesis was more towards a proof of concept and the condyle was not taken into account for these reconstruction implants for simplicity reasons, this version of the SSM was accepted for future steps. However, in further research this should be improved. This could possibly be done by assigning the condyle surface separately with a patch and allowing for a higher number of points on this patch, so more realistic variations in shape and orientations can be detected. In this manner condylar structures can also be compared and used for reconstruction implants.

As reported in table 5, the measurements of the model that was closest to the mean shape were comparable to the measurements of the mean shape of SSM. However, some differences in measurements were observed, like body length and pogonion interdental distance. This could be expected, since every mandible is unique and none would match the mean shape perfectly. The mandibles used for design of the implant base were also included in the database used for the SSM, making the estimation easier. However, this was considered acceptable and it was assumed that models not included in the database would work with similarly. The morphometric measurements taken throughout this thesis were not verified with an oral and maxillofacial surgeon and therefore small mistakes are imaginable. Recommended is that with future research steps of this study, additional revision for the measurements should be made by another researcher, preferable someone with a clinical background.

The measurements of SSM of this thesis versus those of literature [8] were similar as well, except for body height and pogonion interdental distance. This could be attributed to the measurement errors and differences in segmentations of the teeth area. However these two morphological measurements are related to each other. Other SSM studies did not consider

measurements at the symphysis, so further comparison of studies could not be made. To verify the observed variations in figure 11, anatomical measurements related to these variations were taken at the maximum and minimum standard deviations for the first four modes (table 6). These confirmed the variations seen in figure 11. The similar morphological measurements on the mean shape of the SSM and similar variations shown in the modes indicate that the SSM works. Only small adaptions need to take place to make the condyle rightfully included as well.

Only age and gender of the patients were known. Previously known pathologies related to the oral maxillofacial region were not given. Additionally, the origin of these patients were also unknown. It is assumed they are all of Dutch or Caucasian origin, however, this is not verified. In several studies in literature, it is stated that some morphological mandible measurements change within patients from different origins [41-44]. Therefore, we need to assure that no significant differences take place within these origin groups whenever they are mixed in one SSM, else several SSMs need to be made to help patients of all kinds.

SSM can be used for more than just designing reconstruction implants. Another application of SSM in literature is for automatic segmentation of the mandible [35]. Moreover, this model can be used as a guideline for realigning bone fractures in severe mandible situations, such as those in which the mandible is so severely broken that original shape cannot be retrieved without the previous knowledge of the mandible state. SSM in these cases can be used with just a fraction of the remaining bone, or a new SSM should be created including the skull, in which the size and shape of the skull can be used to estimate a well fitted and suited mandible for a patient.

4.2 SHAPE ESTIMATION

Clinicians have suggested using the SSM in cases of large asymmetry. The mandible is an asymmetric bone. Türp et al. [29] state that the asymmetry of the condyle and ramus ought to be taken into account and belong to the biological variation of people. Proper alignment of a mirrored mandible to its normal orientation was not possible and errors in alignment occured, resulting in differences in distance between the point clouds of implant bases created by mirror method and the original missing anatomy of the bone (see figure 14 and 15). Figure 15 reports average differences of up to 3 mm for the mirroring method. Large symmetries such as those in patients of hemifacial microsomia, in which lateral structures of the face are not fully grown or missing at all, could be adapted by implants for the condyle, ramus, body or gonial angle [45]. When fabricating these implants, often mirroring of the healthy side is used, if possible. However, additional to the existing challenges for these case

is that finding a midplane is rather difficult for these patients. This depends on the severity of the hemifacial microsomia, since usually both sides of the face are affected, one often more than the other. Other applications of the SSM include the use small adaptions in plastic surgery to improve physical appearances regarding abnormal mandibular contour shapes, for example the symphysis or gonial angle. In such cases, these designated parts could be manually removed digitally, and the remaining model can then be used with the SSM to generate a more fitting shape of this part of the mandible.

The errors measured as maximum distances between the implants' point cloud and those of the manually removed missing bone part reported in figure 14 and 15, showed that the use of an extruded base resulted in similar small errors for the cases with only 10 percent volume defect. However, when the defect size increased, more than just an extruded base is needed for correct face contours. Results from mirroring techniques and SSM show no significant difference. However as previously mentioned, mirroring techniques has limitations regarding some extreme cases and location of defects. The estimated error that occurs for mirroring method results from asymmetry. In the case of a 25% volume defect for example, the body width can differ due to several reasons including the presence or absence of certain molars. Other differences that can occur are within the body and ramus length and the gonial angle [29, 30, 46]. Additionally, in this thesis study, the SSM was only partially working. Surfaces were rough sometimes and alignment was not optimal. It is expected that the maximum and average distances would be improved whenever this SSM is adapted.

4.3 IMPLANT DESIGN

The final implant created is a simplified version of a reconstruction implant. It only covers the main basis for the design of a partial mandible reconstruction implant. The choice for this kind of implant was partly because no muscle attachments were present on the selected reconstruction section. However, in reconstruction cases of larger defects or sections including the condyle or ramus, muscle attachments might be included. It is important to investigate what happens to the muscle attachments side. Muscles should always be saved if possible, to restore the ability of all movements needed for mastication and speech. Additionally, asymmetric muscle activity occurs within patients with mandible asymmetry [47] and should be taken into account for the FEM with severe asymmetry.

In cases of bone tumors, surrounding soft tissue is also removed for safety reasons. This includes blood vessels, nerve endings, muscles, fat tissue and skin. In these cases, more than a metal implant is needed for good reconstruction of the face. This is similar in cases of

severe trauma (*e.g.* gun wounds) in which a free flab auto graft including skin, or a face transplant, is currently needed to restore some function and appearance.

Additionally, features like teeth implants and the interface between the bone tissue and the implant are not considered in this study. Additive manufacturing (AM) allows for implants with well controlled pore size [48], which can facilitate for bone ingrowth and drug delivery [49]. Using porous structures with a minimum pore size of a few hundred micrometer can lead to bone tissue reconstruction [50], resulting in a more rigid connection between the bone and the implant. Topology optimization on the local structures of the implant can be completed, to create structures that match the mechanical properties of bone better [51], thereby minimizing stress shielding [48]. In this study, merely the global topology optimized base was designed using patient-specific shapes retrieved using the SSM. However, additional features and bone-implant interface should be investigated in further research for optimal implant design. Similarly, the mechanism of how the implant is attached to the bone (*e.g.* screws) needs to be designed. When all of this is taken into account mechanical test can be done to verify computational simulations.

4.4 FINITE ELEMENT MODELING

Equation (7) was originally given as $E = 0.09 + 0.9\rho^{7.4}$ [22]. However, this resulted in extremely high calculated E-values that did not match the HU values that were reported in the paper of [22]. Therefore, the coefficients in equation (7) were modified, so that the HU values and E-values mentioned in [22] were corresponding with each other.

Many assumptions were made within the model. Firstly, the material properties were assigned for 10 sections for both cortical and cancellous bone, creating a total of 20 material properties. However, in reality more variations between HU values might take place. Besides that, the material considered to be isotropic, while other papers sometimes used orthotropic material properties for the mandible[24, 25, 52, 53]. Material properties in other studies with isotropic values for both cancellous and cortical bone, change a lot within literature. Some of the published values for cancellous and cortical bone were 1.37 GPa, and 13.7 GPa [54, 55], 0.79 GPa and 13.7 GPa [56] or 1.5 GPa and 15 GPa [57]. Papers that calculated the material properties with HU values for the mandible, reported mean E-values of 0.68 GPa and 30.1 GPa [22] or varied from 1.53 GPa to 37.6 GPa [58]. Other studies just assigned one material property for bone of 15 GPa [59] or 13.7 GPa [60]. Mean E-values of this thesis study were around 1.0 GPa and 18.5 GPa for cancellous and cortical bone, respectively. This proved that equation 4 to 7 estimated the material properties comparable to literature. A higher E-value for cortical bone in this thesis study can be explained by the assumptions made regarding the

teeth. In the model of this thesis, the teeth were not included. However, the part of the teeth roots were still in the model but segmented as cortical bone by the HU values. Because of this, high cortical bone E-values were assigned in these sections of around 40 GPa. This is between cortical bone and teeth material, since dentin and enamel have a Youngs modulus of 17.6 GPa and 80 GPa [25], respectively. Since the values of the teeth roots were included in the cortical bone calculation for the mean E-value, it is expected to be higher. Also, because of this simplification, the interaction of bone and teeth were not considered for the FEM.

Another assumption was that only four muscles were included, similar to Pinheiro et al. [23]. However some of these muscles have multiple heads and therefore multiple attachments sites. This is visible in the temporalis. Other studies [24, 25] modelled these muscles as anterior, middle and posterior temporalis muscles, however all forces were relatively small. Other muscles in Korioth's [24, 25] study were the anterior digastric muscles. However, these muscle is not primarily used in mandible movements and muscle forces were negligible.

The extremely high values of the stresses that occur at the incision bite were probably because of the small incision constraint. The forces of the muscles should account for a biting force of 570.9 N or 600.4 N [23] for the biting tasks used, however in reality this is not assigned to a few nodes. Additionally, the load should be applied on the enamel of the teeth and transferred through the dental part and the teeth roots, making the load transfer to the bone more widely distributed. Another boundary condition included total fixation of the top surface of the condyles. However, as previously mentioned, the TMJ is a ginglymoarthrodial joint. In this case fixation was chosen, assuming the joint did not move during the clenching task.

Since every mandible is unique, comparison is not always feasible. Additionally, many studies investigated different biting tasks or a no-mastication or a neutral position was modelled [59]. To verify the FEM results for displacement and stress, a comparison with literature which used similar muscle forces [23-25] was done.

The maximum stress for INC in the intact mandible in [23] reached approximately 36 MPa at the anterior border of the coronoid process, 58 MPa directly underneath the condyle and 56 MPa at the mandibular notch. Similar values were found at the healthy model in this thesis (figure 17) for the posterior border of the ramus and the neck of the condyle. However, no extra stress concentrations occurred at the anterior border of the coronoid process. In the healthy intact model of this thesis study, extra stress concentrations were found in two regions, the posterior border of the ramus and at the alveolar, were the teeth sockets are. An

explanation for this could be that teeth were not included, causing different stress contribution patterns in these areas. Other higher stress concentrations were created at muscle force attachment sites and boundary condition sections, however these were not investigated and assumed to be caused by to the assignment techniques of muscles in the FEM.

Pinheiro et al. [23] also stated that since the muscle forces are applied in equal amounts on both left and right side in INC, displacement should be symmetric. However, this was not seen in this study (figure 19). Displacement was slightly in left lateral direction. This could be explained due to asymmetry of the bone, since the ramus height on the left side is larger and body width is not equal around the third molar sections. Another asymmetry that occurred was due to position, since seemed that the left and right TMJ were not at the same vertical height. Due to this, small uneven displacements can occur. Displacement patterns were similar as those presented in [23, 25]. The mandible moved inwards posteriorly, this displacement decreased anteriorly. In vertical direction the healthy mandible moved upwards. However this amount decreased when moving from the gonial angle to the symphysis.

In the RMB model of the previous study [23, 25] slight movements in transverse direction occurred. The mandibles showed greater displacements were on opposite side of the bite. Hence in RMB, this should occur at the left side of the mandible, which is the case in the healthy model (figure 21). Other observations were upward and forward movements, which were larger on the left side compared to the right side. Likewise [23] reported that larger stresses occurred posteriorly at the ramus located at the opposite side of the biting task, also seen in figure 21 where a von Mises stress of around 25 MPa was found. Therefore, the healthy model in RMB loading conditions were rightfully simulated.

The model including the solid implant can be compared to the healthy situation. Due to larger mesh size of the implant-based model, small differences can occur in the geometry (*e.g.* volume and surface decreased with 1%). Displacements in the model with solid implant (figure 20) were similar in the vertical plane when compared to the healthy mandible (figure 19). However, in the anterior plane displacements were different. In the model with the implant, displacements occurred to the right side, while in the healthy intact model displacement, was to the left side in the anterior plane. Displacement to the right for the implant model are due to high stiffness of the solid titanium alloy implant, reducing displacements to the implant's side.

4.5 TOPOLOGY OPTIMIZATION

Results shown in figure 27, 28 and 29 illustrated that the full processes from using SSM to creating a light weight implant with topology optimization is possible. The globally topology optimized implant was able to preserve the contours of the missing anatomy part. The implants were relatively light weight, under 25 grams. However, extra teeth implants and the attachments to bone will provide additional weight. Although, as a proof of concept for design of the base of the implant, the project can be deemed successful.

Firstly, the topology optimization was calculated for different volume constraints, to see if small changes within volume had effect on the shape. The crossing within the implant with a higher volume constraint of 0.24 (figure 25) compared to those with the minimal volume constraint of 0.2 (figure 24) suggested that the volume constraint had an influence on the shape in a small amount. The crossing still occurred at the lateral inferior side of the implant and only slight anterior changes occurred. Similar stresses of around 300 MPa were obtained within the implant, which is way below the maximum compressive stress of 850-1050 MPa of Ti6Al4V. Displacement patterns of the mandible shifted back to the left lateral side, similar to the healthy mandible model, suggesting that topology optimized implant allows for the maintenance of the stress and displacement distribution of the mandible. The similar location frames (figure 31), suggests that the right biting task accounts for similar strain patterns within the mandible.

The topology optimized implant models were investigated under the opposite boundary conditions. The TI_INC under RMB conditions (figure 30) showed similar results as the TI_RMB under these conditions (figure 26). Similar displacement patterns occurred at the left gonial angle and only slightly higher stresses occurred at the implant. This could be explained due to the smoothing and remeshing, which caused the implant to reduce slightly in size, resulting in higher stresses. Measurements taken with three different regions (figure 34) were similar within the condylar neck in this case to the healthy mandible. Mean von Mises stresses in the coronoid process and gonial angle were similar too.

The TI_TMB under INC (figure 33) however created higher von Mises stresses all over the implant of around 450 MPa and extreme high values around the connection between bone and the implant. For this case smoothing and remeshing could have caused higher concentrations. However, values of over 2000 MPa, indicate that the use of the TI_RMB will fail under extra loading conditions like INC. Also, displacement of figure 33 revealed a different pattern as those for healthy and the implant made under INC, suggesting that using

the TI_TMB does not allow for maintenance of the stress and displacement distribution of the mandible.

The average stresses in condylar neck, coronoid process and gonial angle are shown in figure 33. Stresses during the INC task, which were between 8 and 50 MPa, were higher compared to stresses during the RMB task, which were in between 5 and 20 MPa. The stress-strain curve of Mow & Hayes [61] shows that the cortical bone will fracture above 160 MPa, which is above all our average stress in this study, but below some of the maximum stresses (table 8) within the condylar neck during INC. However, since similar high stress occur in the intact healthy mandible, it is suggested that these values are related to assumptions made for FEM. This might be due to the section assignment for the material properties using HU values. Porous structures within the mandible, which occur at the gonial angle and condylar neck, were assigned with the lower limit of density and minimal E-value (ρ=0.105 g/cm^3 and E=0.06 GPa). However in reality this would be porous, resulting in slightly different behavior. Other reasons might be the smaller incision areas for the teeth or related to the muscle force assignment.

Topology optimization with an implant with pores previously assigned to it (figure 33) in comparison to the same mandible with similar loading conditions and volume constraint resulted in a slightly different frame. However, this was still located at the same region of the implant. This suggests that the assignment of pores for whatever reason (*e.g.* implants, blood vessels etc) caused changes in the final design and should have been taken into account before topology optimization was assigned.

The outcome of the FEM with topology optimization for extreme cases of the mandible shape (figure 30) illustrated that the obtained implant frame was very different between the two patients and between the mean shape previously investigated. This suggests that the designed frame for the base of the mandible reconstruction implant is patient-specific. For the FEM of all three patients the same muscle forces were used. However, these muscle forces can be influenced by skull/mandible size and by gender. More investigations have to be carried out to see what changes in muscles forces need to take place, before adaption within the simulation can be made. With adapted muscle forces, a patient-specific loading can be created. This can include extra information when muscles are less present or removed entirely due to, for example trauma or disease.

Another way to use this workflow could be by using the results as a surrounding case in auto graft surgery, if more soft tissue is needed. Using these patient-specific outcomes of the SSM, the frame can still be used, but filled with bone tissue (*e.g.* from the fibula or iliac bone). The

bone might be able to take up loads and maybe other biocompatible materials can be used. This way additional tissues, such as blood vessels, bone or skin can be added. While a good realistic contour of the mandible can still be created using the SSM for estimating the mandible shape, both the superior and inferior borders have benefits like holding teeth implants and improving physical appearance of a patients face.

Finally, it is important to mention that all segmentations and modifications using both software of Materialize (*e.g.* Mimics and 3-Matic) (version 21.0, Materialise, Leuven, Belgium) and fabrication of the FEM using ABAQUS, version 2017 (Dassault systems, Vélizy-villacoublay, France) were made by one person. Intra observer variations were not considered, however this subjectively can occur (*e.g.* with measurements). With future research, all data should be verified by a second or third person, preferable one with a clinical background, and inter observer testing should be done. However, in the time frame of this thesis, this was not possible.

5

CONCLUDING REMARKS

5.1 CONCLUSION

This thesis project can be considered a proof of concept for the design and optimization of patient-specific implants for mandible reconstruction, which can easily be manufactured using additive manufacturing processes. With the use of 35 segmented mandibles models, the SSM was generated using unbiased registration on the mandible point clouds and principal component analyses. This was done to extract the mean shape, mode shape variations and the shape parameters. One SSM was created regardless of the gender, since no statistical significance was found between male and female variations. Missing shapes of the mandible for four different defect scenarios were estimated separately using this SSM, an extrude base and mirroring of the healthy intact side. Calculations made of the average and maximum distances between the point clouds of the missing part and the estimated shape showed that with larger defect sizes, an extruded base was not sufficient enough to estimate the missing anatomy part. The maximum and average distances for SSM and mirroring methods were similar, no significance was found. However due to limitations of the mirroring method (*e.g.* no symmetry and dependent on location of defect) and the promising ability to optimize the SSM, the SSM was assumed to be superior. The 25% volume defect implant was slightly manually adapted to create the final solid implant used in further modelling. Comparable stress distributions and displacements in the healthy intact mandible to those of literature verified the correct use of the simulation. Therefore, FEM with similar loading conditions was made to the model with a 25% total volume defect and a solid Ti-alloy implant. Topology optimization for different volume constraints showed small changes, however location of the frame occurred at the same regions of the implant. Similar conclusions were found for different clenching tasks. Starting the topology optimization in which the initial implant was porous, resulted in a different frame. However, this was still located at the same region of the implant as the other outcomes for topology optimization of

that mandible. Repeated FEM on different extreme patient cases suggested that the topology optimized frame is patient-specific.

From this project it can be concluded that the semi-automatic workflow of designing the frame of a light-weight implant for partial mandible reconstruction surgery can be created using a SSM and topology optimization. This results in patient-specific outer contours for good physical aesthetics and patient-specific topology optimized global structures that can be used as a base for partial mandible reconstruction implants.

5.2 FUTURE RECOMMENDATIONS

Future recommendations include improvements of the MATLAB scripts used for both, the design and alignment of the SSM. To improve the implant for mandible reconstruction purposes, additional features should be included, and investigations should take place to study the interactions of bone tissue and implants. Additionally, more mandible cases can be modelled with adapted muscle forces, to see if changes occur within the globally optimized shape.

The workflow used in this study can be used proof of concept. It can also be adapted for different implant purposes, regarding other anatomical bones within the human body. The full body CT-database used in this study could facilitate many more SSM, which will have a great influence in the fabrication of additively manufactured patient-specific implants.

REFERENCES

[1] J. Tuomi *et al.*, "A novel classification and online platform for planning and documentation of medical applications of additive manufacturing," vol. 21, no. 6, pp. 553-559, 2014.

[2] M. Javaid and A. Haleem, "Additive manufacturing applications in medical cases: A literature based review," *Alexandria Journal of Medicine,* vol. 54, no. 4, pp. 411-422, 2018/12/01/ 2018.

[3] E. N. Marieb and K. Hoehn, *Human anatomy & physiology*. Pearson Education, 2007.

[4] A. Osborn, W. H. Hanafee, and A. A. J. A. J. o. R. Mancuso, "Normal and pathologic CT anatomy of the mandible," vol. 139, no. 3, pp. 555-559, 1982.

[5] M. M. Helland, "Anatomy and Function of the Temporomandibular Joint," vol. 1, no. 3, pp. 145-152, 1980.

[6] L. Guarda-Nardini, D. Manfredini, and G. Ferronato, "Temporomandibular joint total replacement prosthesis: current knowledge and considerations for the future," *International Journal of Oral and Maxillofacial Surgery,* vol. 37, no. 2, pp. 103-110, 2008/02/01/ 2008.

[7] X. Alomar *et al.*, "Anatomy of the Temporomandibular Joint," *Seminars in Ultrasound, CT and MRI,* vol. 28, no. 3, pp. 170-183, 2007/06/01/ 2007.

[8] R. Vallabh, J. Zhang, J. Fernandez, G. Dimitroulis, D. C. J. B. Ackland, and m. i. mechanobiology, "The morphology of the human mandible: A computational modelling study," pp. 1-16, 2019.

[9] B. T. Goh, S. Lee, H. Tideman, P. J. J. I. j. o. o. Stoelinga, and m. surgery, "Mandibular reconstruction in adults: a review," vol. 37, no. 7, pp. 597-605, 2008.

[10] P. Boffano, S. Kommers, K. Karagozoglu, C. Gallesio, T. J. I. j. o. o. Forouzanfar, and m. surgery, "Mandibular trauma: a two-centre study," vol. 44, no. 8, pp. 998-1004, 2015.

[11] M. J. Busuito, J. D. Smith, and M. C. J. T. J. o. t. Robson, "Mandibular fractures in an urban trauma center," vol. 26, no. 9, pp. 826-829, 1986.

[12] S. Lonie, P. Herle, A. Paddle, N. Pradhan, T. Birch, and R. J. A. j. o. s. Shayan, "Mandibular reconstruction: meta-analysis of iliac-versus fibula-free flaps," vol. 86, no. 5, pp. 337-342, 2016.

[13] I. T. Jolliffe, N. T. Trendafilov, M. J. J. o. c. Uddin, and G. Statistics, "A modified principal component technique based on the LASSO," vol. 12, no. 3, pp. 531-547, 2003.

[14] M. P. Bendsøe, "Topology optimizationTopology Optimization," in *Encyclopedia of Optimization*, C. A. Floudas and P. M. Pardalos, Eds. Boston, MA: Springer US, 2009, pp. 3928-3929.

[15] J. S. Brown, C. Barry, M. Ho, and R. Shaw, "A new classification for mandibular defects after oncological resection," *The Lancet Oncology,* vol. 17, no. 1, pp. e23-e30, 2016/01/01/ 2016.
[16] M. L. Urken *et al.*, "Oromandibular reconstruction using microvascular composite free flaps: report of 71 cases and a new classification scheme for bony, soft-tissue, and neurologic defects," vol. 117, no. 7, pp. 733-744, 1991.
[17] N. Tümer *et al.*, "Bone shape difference between control and osteochondral defect groups of the ankle joint," *Osteoarthritis and Cartilage,* vol. 24, no. 12, pp. 2108-2115, 2016/12/01/ 2016.
[18] N. Tümer *et al.*, "Three-dimensional analysis of shape variations and symmetry of the fibula, tibia, calcaneus and talus," vol. 234, no. 1, pp. 132-144, 2019.
[19] N. Tümer, G. Vuurberg, L. Blankevoort, G. M. M. Kerkhoffs, G. J. Tuijthof, and A. A. J. J. o. O. R. Zadpoor, "Typical Shape Differences in the Subtalar Joint Bones Between Subjects with Chronic Ankle Instability and Controls," 2019.
[20] M. Van De Giessen, F. M. Vos, C. A. Grimbergen, L. J. Van Vliet, and G. J. Streekstra, "An efficient and robust algorithm for parallel groupwise registration of bone surfaces," in *International Conference on Medical Image Computing and Computer-Assisted Intervention*, 2012, pp. 164-171: Springer.
[21] D. J. O. S. P. Girardeau-Montaut, "Cloud compare—3d point cloud and mesh processing software," 2015.
[22] M. Ay, T. Kubat, C. Delilbasi, B. Ekici, H. E. Yuzbasioglu, and S. J. U. U. J. o. M. S. Hartomacioglu, "3D Bio-CAD modeling of human mandible and fabrication by rapid-prototyping technology," p. 135, 2013.
[23] M. Pinheiro and J. J. J. o. C.-M. S. Alves, "The feasibility of a custom-made endoprosthesis in mandibular reconstruction: implant design and finite element analysis," vol. 43, no. 10, pp. 2116-2128, 2015.
[24] T. W. Korioth, D. P. Romilly, and A. G. J. A. J. o. P. A. Hannam, "Three-dimensional finite element stress analysis of the dentate human mandible," vol. 88, no. 1, pp. 69-96, 1992.
[25] T. Korioth and A. J. J. o. D. R. Hannam, "Deformation of the human mandible during simulated tooth clenching," vol. 73, no. 1, pp. 56-66, 1994.
[26] V. Ferrario, C. Sforza, G. Serrao, C. Dellavia, and G. J. J. o. o. r. Tartaglia, "Single tooth bite forces in healthy young adults," vol. 31, no. 1, pp. 18-22, 2004.
[27] P.Sheweta and A. Mariamichael, *Finite element analysis of the skull implant using ANSYS software*. 2011.
[28] T. D. Ngo, A. Kashani, G. Imbalzano, K. T. Q. Nguyen, and D. Hui, "Additive manufacturing (3D printing): A review of materials, methods, applications and challenges," *Composites Part B: Engineering,* vol. 143, pp. 172-196, 2018/06/15/ 2018.

[29] J. C. Türp, K. W. Alt, W. Vach, and K. J. C. Harbich, "Mandibular condyles and rami are asymmetric structures," vol. 16, no. 1, pp. 51-56, 1998.
[30] G. Captier, J. Lethuilier, M. Oussaid, F. Canovas, F. J. S. Bonnel, and R. Anatomy, "Neural symmetry and functional asymmetry of the mandible," vol. 28, no. 4, pp. 379-386, 2006.
[31] M. I. Mohammed, A. P. Fitzpatrick, and I. Gibson, "Customised design of a patient specific 3D printed whole mandible implant," in *DesTech 2016: Proceedings of the International Conference on Design and Technology*, 2017, pp. 104-111: Knowledge E.
[32] S.-G. Kim *et al.*, "Development of 3D statistical mandible models for cephalometric measurements," *Imaging Sci Dent,* vol. 42, no. 3, pp. 175-182, 9/ 2012.
[33] S. Raith *et al.*, "Planning of mandibular reconstructions based on statistical shape models," *International Journal of Computer Assisted Radiology and Surgery,* vol. 12, no. 1, pp. 99-112, 2017/01/01 2017.
[34] M. C. Metzger *et al.*, "Anatomical shape analysis of the mandible in Caucasian and Chinese for the production of preformed mandible reconstruction plates," *Journal of Cranio-Maxillofacial Surgery,* vol. 39, no. 6, pp. 393-400, 2011/09/01/ 2011.
[35] S. T. Gollmer and T. M. Buzug, "Fully automatic shape constrained mandible segmentation from cone-beam CT data," in *2012 9th IEEE International Symposium on Biomedical Imaging (ISBI)*, 2012, pp. 1272-1275.
[36] S. Seo, M. K. Chung, B. J. Whyms, and H. K. Vorperian, *Mandible shape modeling using the second eigenfunction of the Laplace-Beltrami operator* (SPIE Medical Imaging). SPIE, 2011.
[37] S. Zachow, H. Lamecker, B. Elsholtz, and M. Stiller, "Reconstruction of mandibular dysplasia using a statistical 3D shape model," *International Congress Series,* vol. 1281, pp. 1238-1243, 2005/05/01/ 2005.
[38] S. Hegde, B. Praveen, and S. J. D. Shetty, "Morphological and radiological variations of mandibular condyles in health and diseases: a systematic review," vol. 3, no. 1, p. 154, 2013.
[39] S. H. Yale, B. D. Allison, and J. J. O. S. Hauptfuehrer, Oral Medicine, Oral Pathology, "An epidemiological assessment of mandibular condyle morphology," vol. 21, no. 2, pp. 169-177, 1966.
[40] M. Eisenburger, B. Haubitz, R. Schmelzeisen, S. Wolter, and H. J. A. o. o. b. Tschernitschek, "The human mandibular intercondylar angle measured by computed tomography," vol. 44, no. 11, pp. 947-951, 1999.
[41] Y. Gu, J. A. McNamara, Jr, L. M. Sigler, and T. Baccetti, "Comparison of craniofacial characteristics of typical Chinese and Caucasian young adults," *European Journal of Orthodontics,* vol. 33, no. 2, pp. 205-211, 2010.

[42] S. Y. Shalhoub, O. A. Sarhan, and H. S. Shaikh, "Adult Cephalometric Norms for Saudi Arabians with a Comparison of Values for Saudi and North American Caucasians," *British Journal of Orthodontics,* vol. 14, no. 4, pp. 273-279, 1987/11/01 1987.
[43] D. H. Enlow, C. Pfister, E. Richardson, and T. Kuroda, "An Analysis of Black and Caucasian Craniofacial Patterns," *The Angle Orthodontist,* vol. 52, no. 4, pp. 279-287, 1982/10/01 1982.
[44] N. Ishii, T. Deguchi, and N. P. Hunt, "Craniofacial differences between Japanese and British Caucasian females with a skeletal Class III malocclusion," *European Journal of Orthodontics,* vol. 24, no. 5, pp. 493-499, 2002.
[45] C. Lauritzen, I. R. Munro, R. B. J. S. j. o. p. Ross, and r. surgery, "Classification and treatment of hemifacial microsomia," vol. 19, no. 1, pp. 33-39, 1985.
[46] J. Duthie, D. Bharwani, R. H. Tallents, R. Bellohusen, and L. Fishman, "A longitudinal study of normal asymmetric mandibular growth and its relationship to skeletal maturation," *American Journal of Orthodontics and Dentofacial Orthopedics,* vol. 132, no. 2, pp. 179-184, 2007/08/01/ 2007.
[47] Y. Dong, X. M. Wang, M. Q. Wang, and S. E. Widmalm, "Asymmetric muscle function in patients with developmental mandibular asymmetry," vol. 35, no. 1, pp. 27-36, 2008.
[48] N. Taniguchi *et al.*, "Effect of pore size on bone ingrowth into porous titanium implants fabricated by additive manufacturing: An in vivo experiment," *Materials Science and Engineering: C,* vol. 59, pp. 690-701, 2016/02/01/ 2016.
[49] A. A. Zadpoor and J. J. A. o. B. E. Malda, "Additive Manufacturing of Biomaterials, Tissues, and Organs," journal article vol. 45, no. 1, pp. 1-11, January 01 2017.
[50] A. A. Zadpoor, "Bone tissue regeneration: the role of scaffold geometry," *Biomaterials Science,* 10.1039/C4BM00291A vol. 3, no. 2, pp. 231-245, 2015.
[51] A. Zadpoor, "Current trends in metallic orthopedic biomaterials: from additive manufacturing to bio-functionalization, infection prevention, and beyond," ed: Multidisciplinary Digital Publishing Institute, 2018.
[52] J. Al-Sukhun, C. Lindqvist, M. J. J. o. B. M. R. P. A. A. O. J. o. T. S. f. B. Helenius, The Japanese Society for Biomaterials,, T. A. S. f. Biomaterials, and t. K. S. f. Biomaterials, "Development of a three-dimensional finite element model of a human mandible containing endosseous dental implants. II. Variables affecting the predictive behavior of a finite element model of a human mandible," vol. 80, no. 1, pp. 247-256, 2007.
[53] A. Choi, B. Ben-Nissan, and R. J. A. D. J. Conway, "Three-dimensional modelling and finite element analysis of the human mandible during clenching," vol. 50, no. 1, pp. 42-48, 2005.

[54] A. Boccaccio, L. Lamberti, C. Pappalettere, A. Carano, and M. J. J. o. b. Cozzani, "Mechanical behavior of an osteotomized mandible with distraction orthodontic devices," vol. 39, no. 15, pp. 2907-2918, 2006.
[55] H. Meijer, F. Starmans, F. Bosman, and W. J. J. o. o. r. Steen, "A comparison of three finite element models of an edentulous mandible provided with implants," vol. 20, no. 2, pp. 147-157, 1993.
[56] E. Tanaka, K. Tanne, M. J. M. e. Sakuda, and physics, "A three-dimensional finite element model of the mandible including the TMJ and its application to stress analysis in the TMJ during clenching," vol. 16, no. 4, pp. 316-322, 1994.
[57] T. Nagasao, M. Kobayashi, Y. Tsuchiya, T. Kaneko, and T. J. J. o. C.-M. S. Nakajima, "Finite element analysis of the stresses around endosseous implants in various reconstructed mandibular models," vol. 30, no. 3, pp. 170-177, 2002.
[58] P. Aquilina, U. Chamoli, W. C. H. Parr, P. D. Clausen, and S. Wroe, "Finite element analysis of three patterns of internal fixation of fractures of the mandibular condyle," *British Journal of Oral and Maxillofacial Surgery,* vol. 51, no. 4, pp. 326-331, 2013.
[59] E. Kavanagh, C. Frawley, G. Kearns, F. Wallis, T. McGloughlin, and J. J. I. j. o. m. s. Jarvis, "Use of finite element analysis in presurgical planning: treatment of mandibular fractures," vol. 177, no. 4, pp. 325-331, 2008.
[60] H.-S. Kim, J.-Y. Park, N.-E. Kim, Y.-S. Shin, J.-M. Park, and Y.-S. J. T. j. o. a. p. Chun, "Finite element modeling technique for predicting mechanical behaviors on mandible bone during mastication," vol. 4, no. 4, pp. 218-226, 2012.
[61] W. C. Hayes and V. C. Mow, *Basic orthopedic biomechanics*. Lippincott-Raven Philadelphia, 1997.

APPENDIX A

Table 9: Hounsfield units (HU), density (p), Youngs modulus (E) and number of elements for all 21 material sections for bone for both models. Values are measured from CT-scans in Mimics version 13.0 (Materialize, Belgium) and calculated using equations (4) to (7).

		Healthy Mandible Model				Bone model including the implant			
Material	**#**	**HU**	**Density (*p*) [g/cm³]**	**Young's modulus (E) [Mpa]**	**#elements**	**HU**	**Density (*p*) [g/cm³]**	**Young's Modulus (E) [Mpa]**	**#elements**
Negative HU	1	0	0,1050	69,9	16318	0	0,1050	69,9	4185
Cancellous	1	41,8	0,1844	90,6	23692	41,77895	0,1844	90,6	6058
bone	2	123,4	0,3395	163,7	25397	123,2737	0,3392	163,6	7658
(0< HU	3	205	0,4945	280,1	35964	204,7684	0,4941	279,7	12540
≤815)	4	286,6526	0,6496	439,7	48500	286,2632	0,6489	439,0	14894
	5	368,2	0,8046	642,6	51854	367,7579	0,8037	614,4	15747
	6	449,8	0,9596	888,8	47818	449,2526	0,9586	887,0	13807
	7	531,4	1,1147	1178,2	42594	530,7474	1,1134	1175,7	12169
	8	612,9947	1,2697	1510,9	39226	612,2421	1,2683	1507,6	11454
	9	693,5421	1,4227	1886,9	37023	693,7368	1,4231	1882,7	10745
	10	776,1947	1,5798	2306,1	36284	775,2316	1,5779	2300,9	10716
Cortical bone	1	862,1326	1,6910	9844,0	39941	860,6242	1,6898	9814,7	12058
(HU ≥ 816)	2	952,4057	1,7604	11796,9	40396	949,857	1,7584	11737,9	12639
	3	1042,666	1,8298	14041,9	40855	1039,077	1,8271	13946,8	12941
	4	1132,926	1,8992	16609,0	42108	1128,309	1,8957	16469,4	13561
	5	1223,186	1,9686	19530,5	42035	1217,542	1,9643	19336,5	13543
	6	1313,459	2,0381	22839,8	39453	1528,336	2,2033	22580,4	12322
	7	1403,719	2,1075	26572,7	33952	1395,995	2,1015	26235,6	9780
	8	1493,979	2,1769	30766,5	24845	1485,228	2,1701	30338,1	7085
	9	1584,252	2,2463	35461,0	8850	1574,447	2,2388	34925,9	2530
	10	1674,512	2,3157	40697,4	833	1663,68	2,3074	40038,9	260
TOTAAL	21				717938				216692

APPENDIX B

Figure 39: All 35 mandible models in isotropic view.

Figure 38: All 35 mandible models in anterior view.

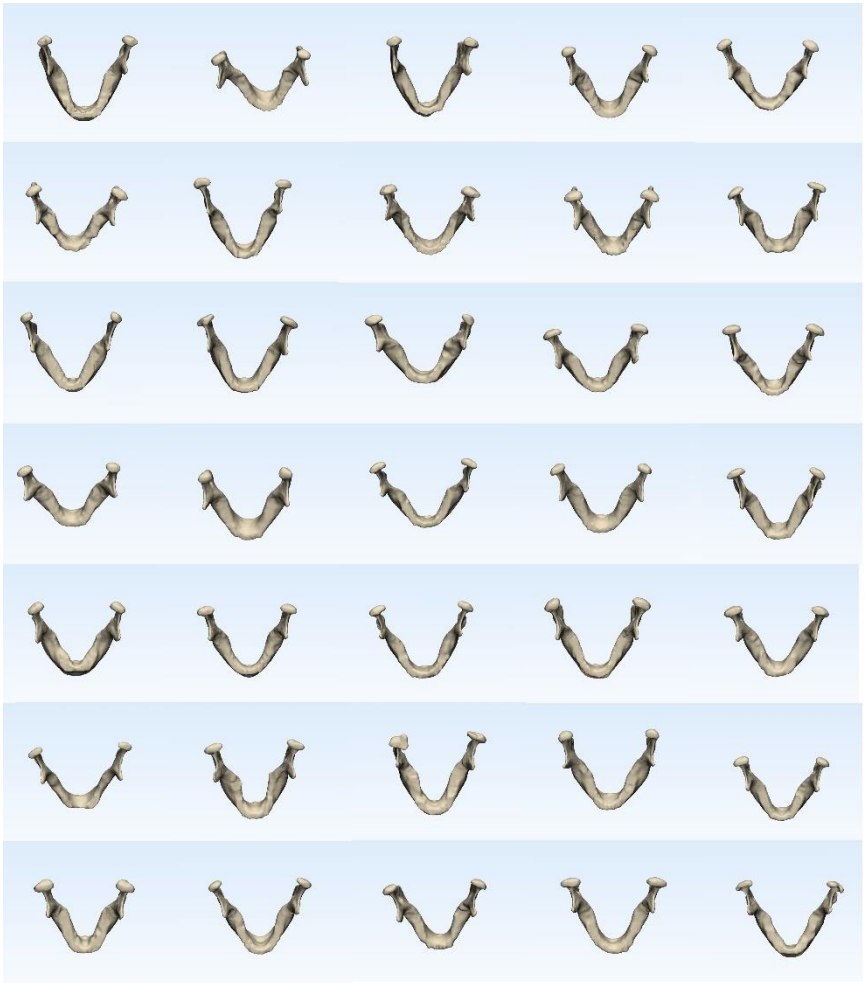

Figure 41: All 35 mandibles in superior view.

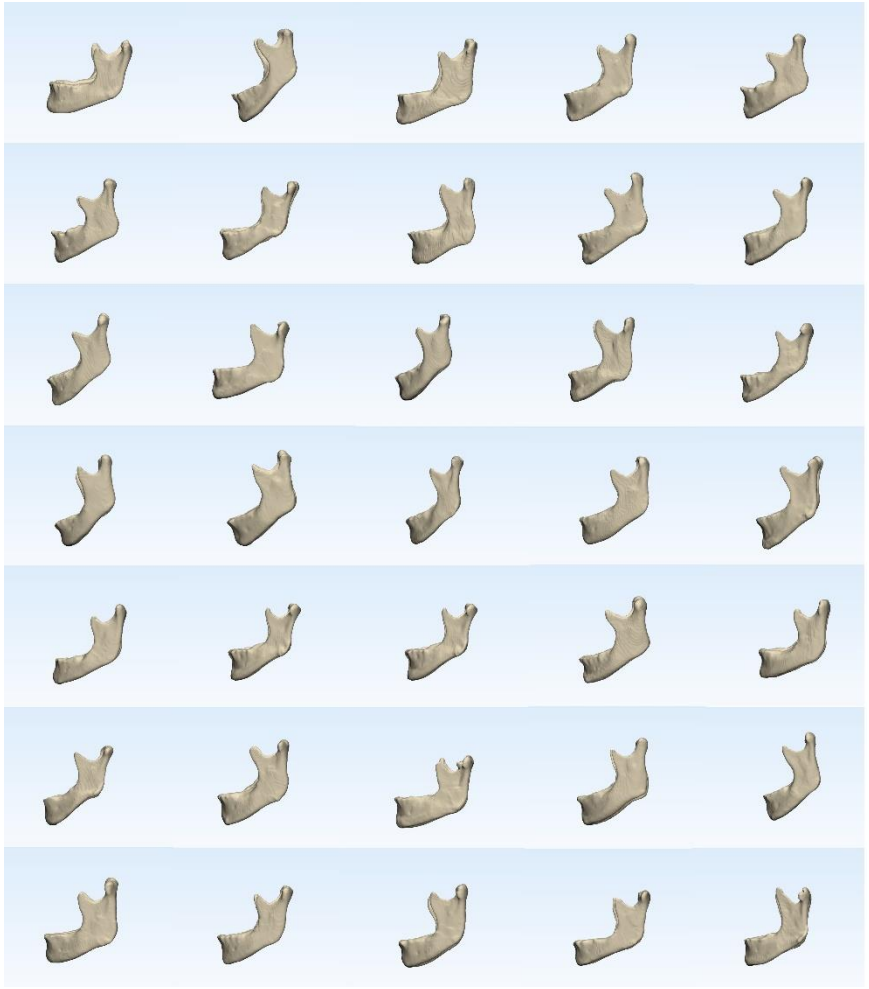

Figure 40: All 35 mandible models in left lateral view.

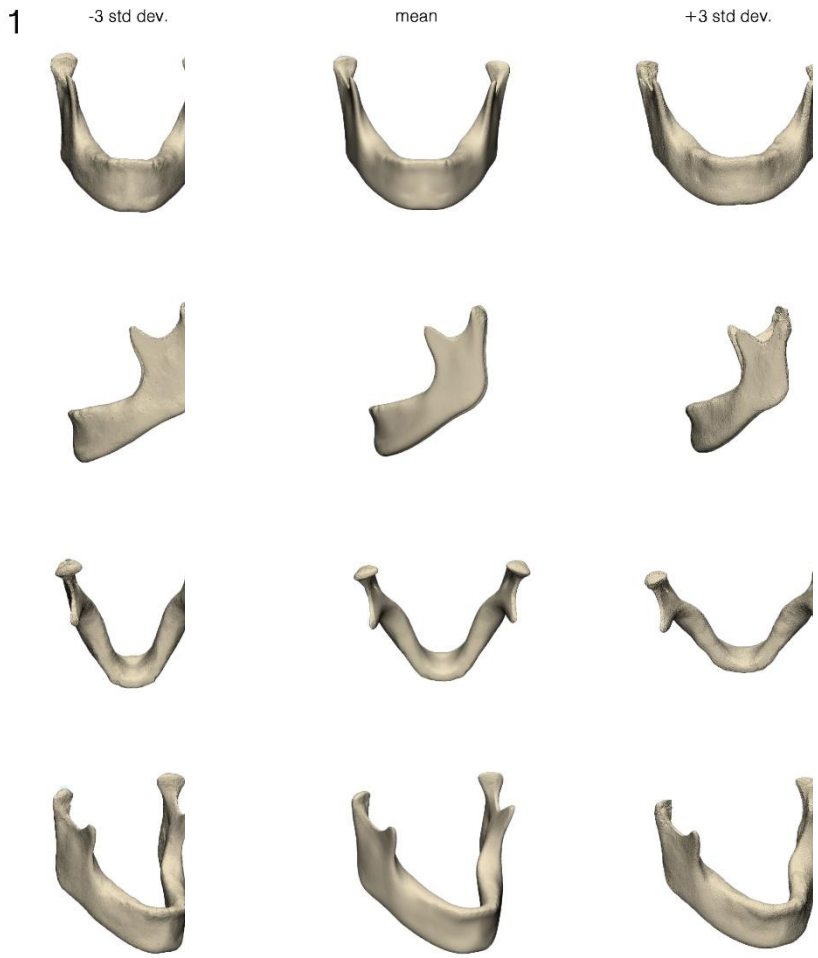

Figure 42: From top to bottom: anterior, lateral, superior and isotropic view of the variations of mode 1 for - 3 standard deviation, mean and +3 standard deviation.

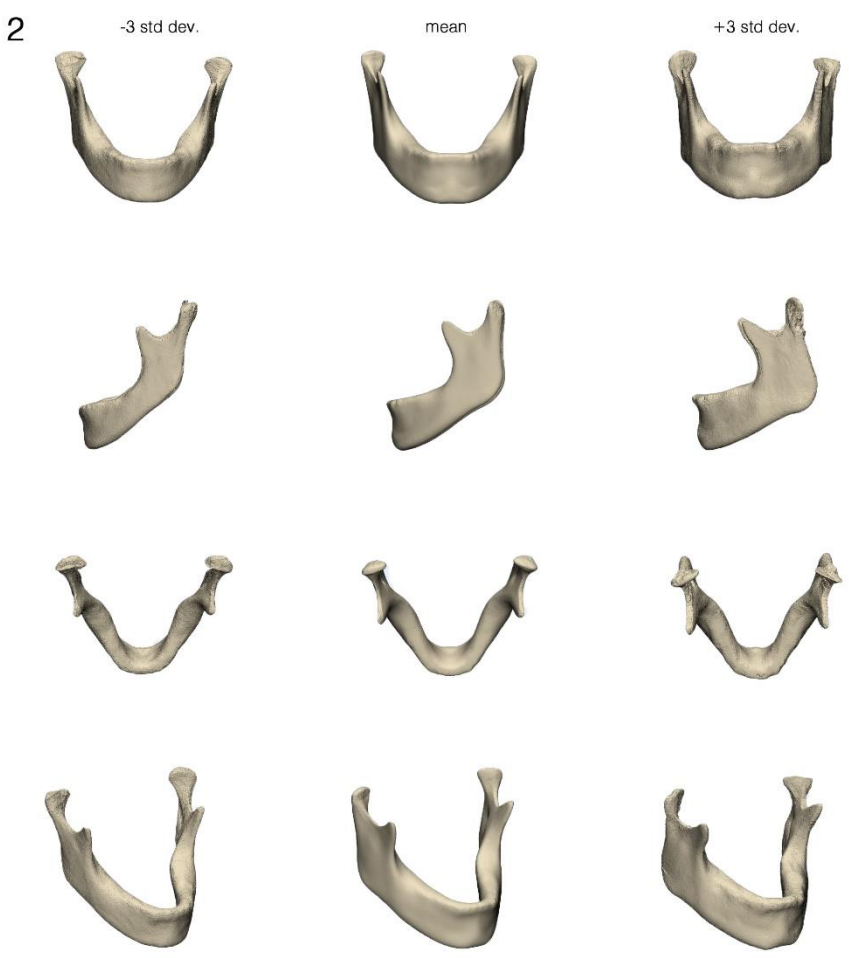

Figure 43: From top to bottom: anterior, lateral, superior and isotropic view of the variations of mode 2 for - 3 standard deviation, mean and +3 standard deviation.

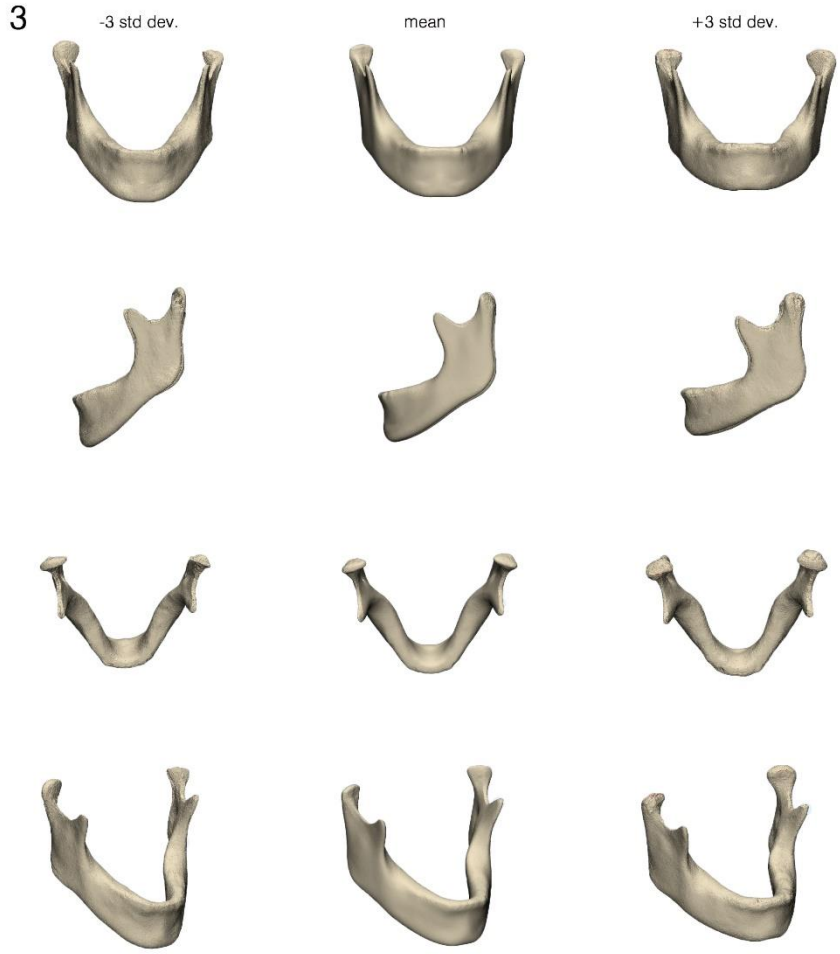

Figure 45: From top to bottom: anterior, lateral, superior and isotropic view of the variations of mode 3 for - 3 standard deviation, mean and +3 standard deviation.

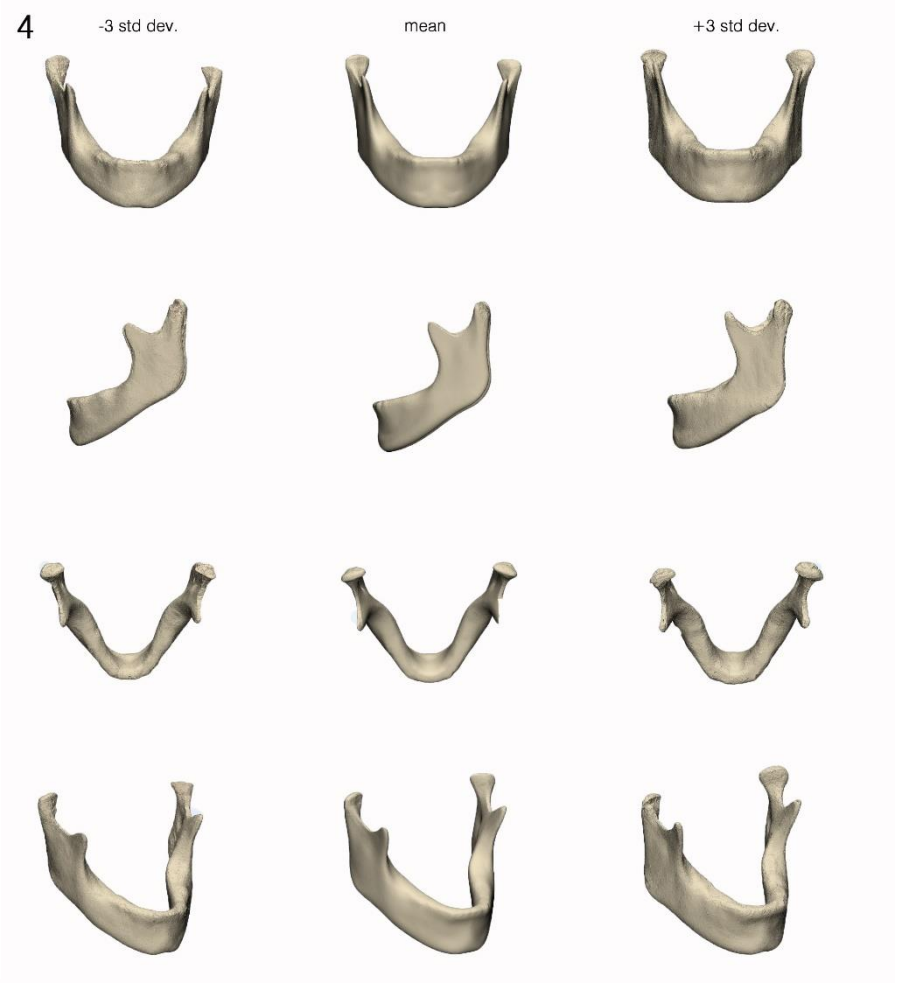

Figure 44: From top to bottom: anterior, lateral, superior and isotropic view of the variations of mode 4 for - 3 standard deviation, mean and +3 standard deviation.

APPENDIX D

Mode	patient																
	1	2	3	4	5	6	7	8	9	10	11	12	13	14	15	16	17
1	-1,24	0,05	0,70	-0,84	2,12	0,75	0,10	1,22	0,72	-0,40	1,95	-0,09	-0,60	-0,14	-0,87	1,04	-0,25
2	-0,84	0,11	-0,03	1,32	-0,86	1,46	-0,47	-0,78	-0,16	-0,29	-1,19	-0,10	0,61	0,36	-1,35	-1,87	-0,26
3	0,77	-0,96	-1,22	-0,10	0,55	-0,72	-1,70	0,71	-0,69	0,39	0,08	0,67	-1,37	0,61	1,44	-1,26	1,97
4	-0,14	0,14	-0,96	-0,40	-0,80	0,86	-1,83	-0,31	0,22	1,75	0,04	-0,57	0,19	0,56	-0,83	2,39	-0,63
5	0,30	-0,97	0,52	-0,49	0,50	-0,29	-1,11	1,20	-2,25	-0,61	0,26	-0,29	0,61	2,33	0,54	0,52	-0,45
6	-1,02	0,19	-0,78	-0,32	0,00	0,40	1,86	1,03	0,75	0,49	0,14	0,28	-0,58	2,09	1,36	-1,27	0,16
7	0,23	0,80	1,26	-0,02	-0,36	-1,28	0,00	1,31	0,17	1,70	-0,36	1,60	-0,62	-0,67	-0,74	1,15	-1,52
8	-0,22	-1,46	0,67	-1,80	0,76	-0,23	0,79	0,08	-0,46	0,72	-1,53	0,21	-0,10	-0,84	-0,33	-0,49	0,75
9	0,05	0,85	0,70	-0,02	-1,31	1,28	0,22	-1,74	-0,03	-1,45	-0,91	1,23	0,35	-0,30	0,66	1,58	0,96
10	-0,14	-1,01	0,65	0,57	1,44	-0,35	-1,09	1,37	0,74	1,50	-0,13	-0,59	-0,53	-0,25	-0,76	-0,37	1,52
11	-0,09	-0,11	1,20	0,20	1,43	0,14	0,18	-0,67	0,05	-1,13	-1,08	-0,89	-0,36	-1,75	0,53	0,73	1,68
12	2,51	1,26	-0,68	0,41	0,28	-1,01	0,28	0,86	-0,07	-0,42	-1,36	0,86	1,66	0,23	-0,29	-0,10	-0,25
13	-0,62	0,80	0,82	0,88	-0,59	-0,43	-2,42	-1,01	-0,03	-0,13	0,38	-0,08	-2,55	-0,07	0,65	-0,46	-0,32
14	-0,44	0,05	-0,29	-1,91	-0,95	-1,94	0,09	-0,80	0,66	0,02	-0,68	0,47	-0,71	0,96	0,53	1,88	1,61
15	-0,88	0,92	0,23	-0,28	0,62	-0,40	0,31	-0,65	1,67	-0,78	-1,11	1,12	-0,49	1,13	0,57	-1,82	-1,56
16	0,94	-0,72	1,50	-1,11	0,44	-0,86	0,57	0,11	1,19	-2,59	1,00	-0,76	-0,39	0,32	0,35	-0,19	-0,61
17	0,71	-1,62	-0,36	0,93	-1,73	-2,50	0,17	0,61	-0,02	-0,60	0,98	0,85	-0,46	-0,45	-0,06	0,31	-1,47
18	-0,70	-0,37	-1,15	-1,08	-1,42	1,41	0,33	1,59	1,38	-0,32	1,74	-0,18	-0,51	-0,52	-1,66	-0,55	0,61
19	-2,11	1,11	-0,18	1,18	0,24	-1,67	-1,38	1,70	2,03	-1,31	-0,88	-1,27	1,64	0,08	0,32	1,12	0,12
20	1,09	1,10	0,81	0,61	0,03	0,59	-0,93	-0,22	-0,04	0,31	1,35	0,42	0,50	1,98	0,58	-0,17	0,92
21	0,29	0,99	-0,36	1,00	0,13	0,28	-0,11	0,03	0,53	1,24	-0,29	-0,34	-1,22	-0,11	-0,66	-0,01	-0,31
22	2,13	-0,58	1,77	-1,40	0,04	1,37	-0,49	0,30	1,47	0,62	-1,17	-0,06	-1,41	0,20	0,16	0,26	-1,47
23	1,21	-0,14	-0,82	-0,89	0,24	-0,84	-0,15	-2,07	0,89	0,64	2,25	-0,70	1,26	-0,49	-0,56	-0,12	0,85
24	-1,55	-1,08	-0,74	-0,58	-0,57	0,66	-0,65	0,13	0,37	0,34	-0,01	1,13	0,07	-0,06	2,41	0,49	0,08
25	-0,69	1,86	-0,36	-0,48	1,60	-0,51	-0,12	-0,17	-0,90	0,87	1,32	1,53	0,12	-2,62	1,71	-0,60	-0,85
26	-0,44	0,81	-0,48	-0,32	0,28	1,17	-0,03	0,55	-0,95	-1,79	-0,24	2,29	-1,36	0,44	-1,20	1,41	0,45
27	-0,11	-1,78	-0,86	1,56	0,32	1,10	1,51	0,77	-1,26	-0,02	-0,47	-0,69	0,08	-0,64	1,42	1,52	-1,11
28	-1,76	-0,37	2,45	-1,38	-0,24	-0,19	-0,97	0,05	-1,81	0,39	0,37	0,80	2,12	0,42	-0,93	-0,76	-0,44
29	-0,43	-0,95	-1,12	-0,48	1,69	0,45	-0,62	-1,88	0,74	0,18	-0,09	-0,42	0,28	1,00	0,58	0,77	-2,35
30	1,12	-0,90	0,61	0,70	-0,41	1,46	-2,26	0,91	0,65	-1,37	0,79	0,30	0,64	-1,39	1,14	-0,45	-0,25
31	0,85	1,87	-1,69	-2,76	-0,71	0,68	-0,85	1,69	-0,69	-0,63	-1,03	-1,19	0,43	-0,84	0,71	-0,51	-0,58
32	0,12	1,53	-0,07	0,41	0,85	-0,51	0,41	0,03	-2,09	-0,90	0,65	-1,93	-1,90	0,64	-0,63	0,36	-0,32
33	-0,52	0,94	2,03	-0,14	-2,38	0,16	1,08	0,39	-0,27	1,13	0,43	-2,13	-0,28	-0,20	1,87	-0,02	0,04
34	-0,20	-0,60	0,13	0,62	-0,97	-0,18	0,40	0,60	0,03	-0,41	0,47	1,41	-0,58	-0,41	-0,54	-0,16	0,34

Table 10: b-values of the SSM for patients 1 – 17 for all 34 modes

		Patient																	
mode		18	19	20	21	22	23	24	25	26	27	28	29	30	31	32	33	34	35
	1	0,32	-2,12	0,99	-1,17	-1,08	0,88	0,68	-1,00	-0,98	-0,32	0,36	-0,22	0,51	0,88	0,82	-2,02	0,45	-1,20
	2	-0,50	-0,35	-1,04	0,78	0,33	0,13	0,64	1,29	-0,45	-1,61	1,40	-0,45	-0,23	1,67	1,72	-1,44	2,04	0,40
	3	1,61	-1,21	-1,49	-0,24	1,19	0,25	-1,79	0,38	-0,63	1,35	-0,01	0,95	0,28	0,47	0,73	-1,19	0,49	-0,29
	4	1,46	-1,00	0,10	1,18	1,34	0,13	0,11	0,59	1,71	-0,47	-0,11	-1,16	0,14	-1,39	-1,54	-1,58	0,65	0,18
	5	0,85	0,07	-1,12	-0,05	-2,86	-1,45	1,07	1,20	0,98	-0,28	0,44	-0,94	0,36	0,69	0,03	0,75	-0,27	0,20
	6	0,25	0,54	0,32	-0,68	-0,46	-0,26	-0,07	0,11	0,81	-2,17	0,21	1,79	-1,82	-0,86	-1,50	-1,63	-0,11	0,78
	7	0,46	0,76	-2,88	-0,45	-0,09	1,73	-0,22	-0,23	0,18	-0,70	-0,03	0,00	-1,83	0,71	0,98	-0,08	-0,94	-0,03
	8	0,08	-1,01	2,31	1,04	0,24	-0,02	-0,52	1,19	1,47	0,60	0,27	-1,15	-2,20	1,20	1,02	-0,32	-1,43	0,70
	9	0,90	-0,49	-0,55	-0,55	-0,59	-0,52	0,11	0,13	-0,54	0,50	1,92	0,88	0,55	-0,11	0,09	-1,70	-2,81	0,65
	10	-1,56	0,48	-0,49	1,23	0,05	0,10	2,07	0,73	-1,54	-0,27	1,04	0,53	0,91	-0,97	-1,41	-0,37	-1,63	-0,29
	11	0,26	1,03	-1,03	1,16	-1,66	0,99	-1,56	-0,55	2,13	-0,94	0,25	0,44	0,24	0,14	-1,09	-0,47	1,63	-1,02
	12	-1,88	-0,91	0,29	0,06	-1,36	0,49	0,34	-0,02	0,54	1,32	-1,58	0,16	0,15	-0,49	-0,07	-2,54	0,69	0,64
	13	0,36	2,04	1,87	-0,10	-1,32	0,65	1,39	0,20	0,11	1,34	-0,58	0,08	-1,14	-0,32	0,60	-1,12	0,45	0,67
	14	-1,12	-0,02	0,52	-0,66	-0,47	1,23	-0,32	1,31	-1,46	-1,71	-0,32	-0,70	1,16	0,29	0,44	0,57	1,30	1,40
	15	1,31	-1,73	-0,36	1,65	-1,00	1,78	-0,10	0,25	-0,22	0,88	0,54	-1,24	0,73	-1,17	-0,81	1,24	-0,19	-0,18
	16	0,59	1,04	-1,07	1,59	2,08	-0,79	0,80	0,48	-0,12	-0,73	-1,51	-0,75	0,37	-0,27	0,71	-1,63	-0,56	0,58
	17	-0,33	-0,32	1,54	1,37	-0,20	0,00	-0,47	0,26	0,69	-0,73	2,46	1,31	0,81	-0,05	0,17	-0,51	0,14	-1,43
	18	-1,01	1,22	-0,99	0,35	-1,47	0,36	-1,52	1,32	0,82	1,66	0,35	-0,50	0,76	-0,74	0,53	-0,19	-0,47	0,92
	19	0,25	-0,21	0,18	-0,02	0,27	-1,55	-1,19	0,09	-0,38	0,77	0,57	0,18	-1,43	0,50	0,18	0,30	0,13	0,62
	20	-1,59	0,79	0,71	1,17	0,06	0,30	-2,28	-0,85	-0,89	-0,84	0,65	-2,31	-0,99	0,25	-0,17	-0,40	-1,10	-1,44
	21	0,87	-0,69	0,68	1,88	-1,44	-1,50	-1,33	-0,47	-0,22	-1,69	-2,11	1,17	1,64	1,11	1,16	0,28	-1,42	0,98
	22	-0,58	-0,26	0,03	-0,56	-0,24	-2,10	-1,04	-0,75	-0,80	0,53	1,49	0,40	-0,33	-0,34	-0,26	0,38	1,83	0,86
	23	0,62	-0,77	-0,91	1,66	-1,51	-0,11	0,97	-0,24	-1,19	0,12	0,54	1,14	-2,35	0,09	-0,20	0,41	0,46	0,73
	24	-2,05	-0,59	-0,96	1,62	0,03	-0,36	1,31	-2,86	1,18	0,23	-0,23	-0,14	0,12	0,16	1,36	0,11	0,12	0,52
	25	-0,63	0,16	-0,25	0,13	0,12	-1,87	-0,30	1,82	-0,21	-0,61	0,79	-1,03	0,61	-0,45	-0,49	-0,59	0,42	0,66
	26	-0,76	-0,41	0,02	1,64	0,47	-0,88	0,32	1,27	-0,64	0,19	-1,10	1,40	-1,63	-0,44	-0,29	1,10	0,77	-1,60
	27	0,72	0,60	0,21	1,20	-0,70	1,05	-0,80	0,23	-2,70	0,36	-0,19	-0,83	-0,76	-1,05	0,37	-0,56	0,45	1,05
	28	0,11	0,47	0,54	0,87	0,28	0,62	-1,39	-0,72	-0,82	0,31	-0,55	1,94	0,75	-0,90	-0,38	-0,46	0,47	1,16
	29	-1,55	0,96	-0,36	-0,17	0,26	0,79	-0,89	1,44	0,13	0,89	-0,35	1,51	0,34	2,23	-0,74	-0,43	-0,88	-0,54
	30	-0,56	-1,60	0,45	-0,89	0,03	1,67	-0,10	1,15	0,41	-1,86	-0,85	0,57	-0,64	-0,17	-0,60	1,22	-0,73	1,20
	31	0,91	1,28	0,74	0,94	0,15	1,06	0,67	-0,80	-0,87	-0,57	0,86	0,47	0,23	1,23	-0,16	0,11	-0,26	-0,75
	32	-1,53	-1,34	-0,51	0,50	1,09	0,98	-0,32	-0,68	0,76	0,29	1,56	0,47	-0,16	-0,05	-0,24	0,45	-0,43	2,49
	33	-0,81	-1,70	-0,57	0,60	-0,21	-0,01	0,24	1,60	-0,34	1,08	-0,99	0,52	-0,08	0,76	-0,56	-0,29	0,23	-1,60
	34	0,44	0,07	0,01	0,41	0,10	-0,25	0,32	-0,97	-0,58	0,67	-0,40	-1,11	0,16	3,26	-3,57	-0,35	0,41	1,43

Table 11: b-values of the SSM for patients 18 – 35 for all 34 modes.

APPENDIX E

Table 12: Maximum distances between point cloud the manually removed part of the mandible to the point cloud of the estimated shape (i.e. extruded base, mirroring or SSM) *for all four defects, measured using cloudcompare.*

		Patient 2	Patient 19	Patient 3	Patient 30	Patient 9
10%	extruded	2,63851	2,78027	5,03482	3,77469	3,1094
	mirror	2,4333	2,7789	2,3617	3,12887	1,40609
	SSM	2,85136	2,68204	1,89747	2,26885	1,61785
16%	extruded	5,5556	4,95217	2,858	7,14646	4,816548
	mirror	-	-	-	-	-
	SSM	3,18528	3,29528	1,54594	2,47625	2,70162
25%	extruded	4,11166	5,3828	5,68162	4,17285	3,01711
	mirror	3,61193	3,65031	4,21554	3,15405	1,51604
	SSM	2,90639	3,65031	2,64218	7,59717	2,78064
50%	extruded	9,19618	15,5882	12,1024	15,875	14,5623
	mirror	6,29255	4,37013	7,04861	5,08803	4,4148
	SSM	7,77428	4,10153	8,58997	8,7531	9,63008

Table 13: Average distances between point cloud the manually removed part of the mandible to the point cloud of the estimated shape (i.e. extruded base, mirroring or SSM) *for all four defects, measured using cloudcompare.*

		Patient 2	Patient 19	Patient 3	Patient 30	Patient 9
10%	extruded	0,387974	0,42071	1,09319	0,949907	0,637319
	mirror	0,350595	0,684781	0,43331	0,904068	0,266705
	SSM	0,61919	0,62119	0,214047	0,43441	0,384437
16%	extruded	1,39546	1,37369	0,630112	1,07086	1,3388
	mirror	-	-	-	-	--
	SSM	0,625245	0,809497	0,343402	0,473426	0,604293
25%	extruded	1,0039700	1,80405	1,0346	0,795522	0,69244
	mirror	0,563482	1,04247	0,782855	0,738894	0,297537
	SSM	0,396373	0,594736	0,794083	1,15268	0,289685
50%	extruded	0,57688	3,34304	2,92562	3,14803	3,15044
	mirror	2,49902	1,12877	2,29102	2,10569	0,797847
	SSM	2,4083	1,10822	2,4994	0,69034	3,28566

APPENDIX F

Table 14: Average and maximum stress measured three selected sections of the left mandible, measured on the healthy bone, one implemented with topology optimized implant created under INC loading (TI_INC) and one implemented with topology optimized implant created under RMB loading (TI_RMB) .

		INC		*RMB*	
		Von Mises Stress [MPa]		Von Mises Stress [MPa]	
		Average	**Max**	**Average**	**Max**
Section 1	Healthy	61,96	298,9	12,88	66,3
Slice at condyle neck	TI_INC	65,77	315,4	13,79	63,28
	TI_RMB	61,96	279,83	13,34	68,3
Section 2	Healthy	9,24	52,92	21,5	129,56
Slice at process	TI_INC	8,676	44,52	8,95	44,86
	TI_RMB	8,360	41,17	8,36	34,28
Section 3	Healthy	18,00	167,47	7,60	41,79
Section @ gonial angle	TI_INC	21,34	79,87	11,13	68,11
	TI_RMB	21,84	110,84	21,96	110,3